이학박사 학위논문

First-principles Study of Electronic, Magnetic and Topological Properties of $CrSiTe_3$ Compounds

$CrSiTe_3$ 화합물의 전자적, 자기적, 위상적 성질에 대한 제일원리 연구

2022년 8월

서울대학교 대학원

물리천문학부

강 성 모

First-principles Study of Electronic, Magnetic and Topological Properties of $CrSiTe_3$ Compounds

$CrSiTe_3$ 화합물의 전자적, 자기적, 위상적 성질에 대한 제일원리 연구

지도 교수 유 재 준

이 논문을 이학박사 학위논문으로 제출함

2022년 8월

서울대학교 대학원

물리천문학부

강 성 모

강성모의 이학박사 학위논문을 인준함

2022년 7월

위 원 장 김 창 영 (인)

부위원장 유 재 준 (인)

위 원 김 기 훈 (인)

위 원 민 홍 기 (인)

위 원 김 홍 식 (인)

First-principles Study of Electronic, Magnetic and Topological Properties of $CrSiTe_3$ Compounds

Sungmo Kang

Supervised by

Professor **Jaejun Yu**

A Dissertation
Submitted to the Faculty of
Seoul National University
in Partial Fulfillment of
the Requirements for the Degree of
Doctor of Philosophy

August 2022

Department of Physics and Astronomy
Graduate School
Seoul National University

Abstract

Study of two-dimensional system is one of interesting subject in condensed matter physics. In recent, observing magnetism in two-dimensional materials attract many people's attention, where transition metal chalcogenides or halogenides have been regarded as one of candidate of magnetic layered materials. $CrSiTe_3$ is one of transition metal tri-chalogenides materials, reported as a ferromagnetic insulator in bulk structure. However, atomically thin structure has never been exfoliated in experiment, where there is controversy in prediction of magnetic states in $CrSiTe_3$ monolayer among theoretical researches. Therefore, we firstly reveal the magnetic ground state of $CrSiTe_3$ by understanding the electronic and magnetic properties using first-priciples study.

In the first part, we investigate the electronic and magnetic structures of two-dimensional transition metal tri-chalcogenide $CrSiTe_3$ and $CrGeTe_3$ materials by carrying out first-principles calculations. The single-layer $CrSiTe_3$ and $CrGeTe_3$ are found to be a ferromagnetic insulator, where the presence of the strong $dp\sigma$-hybridization of Cr e_g -Te p plays a crucial role for the ferromagnetic coupling between Cr ions. We observe that the bandgaps and the interlayer magnetic order vary notably depending on the magnitude of on-site Coulomb interaction U for Cr d electrons. In addition, we find that in-

plane magnetic order in $CrSiTe_3$ monolayer depends on the choice of Hubbard U, where it has ferromagnetic ground state for $U = 1.5$ eV. The bandgaps are formed between the Cr e_g - conduction bands and the Te p valence bands for both $CrSiTe_3$ and $CrGeTe_3$ in the majority-spin channel. The dominant Te p anti-bonding character in the valence bands just below the Fermi level is related to the decrease of the bandgap for the increase of U. We elucidate the energy band diagram, which may serve to understand the electronic and magnetic properties of the ABX_3-type transition metal tri-chalcogenide in general.

In the remaining part, we report Chern insulating phases emerging from single layer of layered chalcogenide $CrSiTe_3$, a transition metal tri-chacogenides materials with layered structure and ferromagnetism, in the presence of charge doping. Due to strong hybridization with Te p orbitals, spin-orbit coupling effect opens finite band gap which leads to nontrivial topology of the Cr e_{g} conduction band manifold with higher Chern numbers. Our calculations show that quantum anomalous Hall states could be realized by adding one electron in unit cell equivalent to electron doping by 2.36×10^{14} cm^{-2} carrier density. We find that the doping-induced anomalous Hall conductivity depends on the spin direction with suppression of magnetic anisotropy energy. Our results show that anomalous Hall conductivity can be controlled by external magnetic field via spin-orientation-dependent tuning of the spin-orbit coupling. We suggest that $CrSiTe_3$ can be a fascinating new platform to realize Chern insulating systems with higher Chern numbers and field controllable quantum anomalous Hall effect.

Keywords: Density functional theory, Two-dimensional system, Transition metal chalcogenides, Ferromagnetism, Berry curvature, Chern insulator, Quantum anomalous Hall effect

Student ID: 2015-20316

Contents

List of Figures

List of Tables

Chapter 1

Introduction

Since the discovery of graphene, two-dimensional (2d) materials have been one of the most intensively studied systems owing to their interesting physical properties as well as chances of applications to atomistic low-power devices[1–3]. Transition metal chalcogenides (TMC) with layered structures is a representative example of such 2d materials[4, 5]. One intensively pursued subject recently in TMC is magnetism originating from the presence of localized magnetic moments in d orbitals at TM ions, where hybridization between TM and chalcogen anions give rise to interesting magnetic behaviours in $X\mathrm{PS}_3$ (X = Mn, Fe, Ni) and $\mathrm{Cr}B\mathrm{Te}_3$ (B = Si, Ge)[6–10]. Systems like $\mathrm{Cr}B\mathrm{Te}_3$ or CrI_3 are reported to show Ising-type magnetism and exhibit magnetic orders down to single-layer limit at finite temperatures[11, 12], defying the Mermin-Wagner theorem that prohibits long range order in systems with d $\leq$ 2 dimensions via thermal fluctuations[13]. Successful exfoliations of atomistically-thin CrI_3 and CrGeTe_3 layers presents promising magnetic 2d system with potential device applications[11, 12].

The presence of robust magnetism in 2d system like $\mathrm{Cr}B\mathrm{Te}_3$ becomes even more interesting in the study of topological properties[14–23], where

TMC materials has been recently considered as one of good platform of researching topological phases of matters[24, 25] and magnetism can be employed as a control knob to tune topological properties in such systems[26–28]. Specifically, quantum anomalous Hall effect (QAHE) can be observed in materials with magnetic ordering and sizable band gap, showing quantized integer Hall conductivity in the absence of external magnetic fields. Chern insulator is one of topological phases of matter showing QAHE characterized by $\mathbf{Z}$ topological invariant, i.e. Chern numbers, unlike time-reversal-symmetric conventional topological insulators classified by $\mathbf{Z}_2$-invariants such as Bi_2Se_3, Bi_2Te_3, Sb_2Te_3[29] or HgTe[30]. Recent studies suggest Chern insulating phases with high Chern numbers and wide bandgap energy[24, 25] can be applied for low-power dissipationless device applications, but exploring suitable candidates is a nontrivial task. $CrSiTe_3$, originally reported to be a 2d ferromagnetic semiconductors with trivial band topology[8, 31–33], can be an ideal candidate in the presence of charge doping because of the robust magnetism and the insulating behavior down to the single-layer limit, in addition due to the presence of strong SOC from Te sites.

Therefore, we study the electronic and magnetic properties of layered transition metal tri-chalcogenide $CrSiTe_3$ and $CrGeTe_3$ materials by carrying out first-principles calculations based on density functional theory. We find that the band gap energy is inversely proportional to Hubbard U value for Cr d electrons. In addition, the interlayer magnetic order also depends on the magnitude of U, where interlayer magnetic interaction energy vanishes near U = 1.0 eV. In $CrSiTe_3$ monolayer, we find that in-plane magnetic order depends on the choice of Hubbard U, where it has ferromagnetic ground state for U = 1.5 eV. Different from general Mott insulating system, the band gap energy

is formed between the Cr e_g - conduction bands and the Te p valence bands for both $CrSiTe_3$ and $CrGeTe_3$ in the majority-spin channel. The dominant Te p anti-bonding character in the valence bands just below the Fermi level is related to the decrease of the bandgap for the increase of U. We elucidate the energy band diagram, which may serve to understand the electronic and magnetic properties of the ABX_3-type transition metal tri-chalcogenide in general.

We also find Chern insulating phases in $CrSiTe_3$ monolayer which can be realized by electron doping. In Cr e_{g} conduction band manifolds, we find crossing points including multiple Dirac cones. They removed by introducing spin-orbit-coupling (SOC) effect, which leads to topologically nontrivial bands with high Chern numbers. We calculate anomalous Hall conductivity (AHC) which is quantized at one- and two-electron-doping per unit cell. We focus on the one electron doping case, where AHC notably depends on spin orientation angle. In addition, the magnetic anisotropy energy is suppressed as electron doping is introduced which makes feasible to control the AHC via external magnetic field. Under one electron doping in unit cell, the calculated magnetic anisotropy energy is 0.289 meV which corresponds to magnetic field as 1.18 T. Our results suggest that ferromagnetic monolayer $CrSiTe_3$ is fascinating materials to realize Chern insulator with high Chern numbers and field controlled quantum anomalous Hall effect under electron doping.

Chapter 2

Computational Method

In this chapter, we briefly review basics of density functional theory (DFT) which is fundamental theory of our research. Firstly, we explain Hohenberg-Kohn theorem, Kohn-Sham equation and exchange-correlation functions with relevant approximations. In addition, DFT+U method for treating on-site Coulomb interaction in localized orbitals and spin-orbit coupling interaction will be discussed. Finally, we will review formalism of maximally localized Wannier functions.

2.1 Density Functional Theory

In solid state physics, the eventual goal is the understanding of electronic states and energies by solving the follwing N-particle Hamiltonian,

$$\begin{aligned} H = &- \sum_I \frac{\hbar^2}{2M_I}\nabla_I^2 + \sum_{I\neq J}\frac{Z_I Z_J e^2}{|\mathbf{R}_I - \mathbf{R}_J|} \\ &- \sum_i \frac{\hbar^2}{2m_e}\nabla_i^2 - \sum_{i\neq I}\frac{Z_I e^2}{|\mathbf{r}_i - \mathbf{R}_I|} + \sum_{i\neq j}\frac{e^2}{|\mathbf{r}_i - \mathbf{r}_j|} \end{aligned} \tag{2.1}$$

where the capital and small letters indicate atomic nucleus and electrons, respectively. In general, nuclei is much heavier than electron so that first two

terms in Eq. (2.1) can be treated as constant by considering Born-Oppenheimer approximation. However, N-electron degree of freedom remain which is hardly solvable in exact. Density functional theory gives approximate solution of this N-electron problem by treating electron densities instead of solving individual electron wavefunctions. Theoretical backgrounds of DFT are discussed in the following sections.

2.1.1 Hohenberg-Kohn Theorem

The Hohenberg-Kohn theorem is one of basic theory of DFT, considering certain systems with electrons influenced by an effective external potential $v_{ext}(\mathbf{r})$[34]. They can be described by following theorem.

Theorem 1 *For non-degenerate systems of interacting particles, the properties of electrons such as Hamiltonian and ground states are determined by electron densities because the effective external potential functional $v_{ext}(\mathbf{r})$ is unique functional for the electron density $n(\mathbf{r})$.*

Proof. If there exist two distinct external potential functional, $v_{ext}^{(1)}(\mathbf{r})$ and $v_{ext}^{(2)}(\mathbf{r})$, which gives equal electron density $n_0(\mathbf{r})$. The corresponding Hamiltonian, $\hat{H}_1$ and $\hat{H}_2$ will thus have distinct wavefunctions of ground states, Ψ_1 and Ψ_2, which give equal electron density $n_0(\mathbf{r})$. Because Ψ_2 is different wavefunction to Ψ_1 which is ground state of Hamiltonian $\hat{H}_1$,

$$\begin{aligned} E_1^0 < \langle \Psi_2 | \hat{H}_1 | \Psi_2 \rangle &= \langle \Psi_2 | \hat{H}_2 | \Psi_2 \rangle + \langle \Psi_2 | \hat{H}_1 - \hat{H}_2 | \Psi_2 \rangle \\ &= E_2^0 + \int n_0(\mathbf{r}) [v_{ext}^{(1)}(\mathbf{r}) - v_{ext}^{(2)}(\mathbf{r})] d\mathbf{r} \end{aligned} \tag{2.2}$$

where E_1^0 and E_2^0 are the energies of $\hat{H}_1$ and $\hat{H}_2$ Hamiltonian ground states, respectively. Same equation is valid for exchanging the subscript 1 and subscript

2,

$$E_2^0 < E_1^0 + \int n_0(\mathbf{r})[v_{ext}^{(2)}(\mathbf{r}) - v_{ext}^{(1)}(\mathbf{r})]d\mathbf{r}. \tag{2.3}$$

If we aggregate Eq. (2.2) and Eq. (2.3), we get $E_1^0 + E_2^0 < E_1^0 + E_2^0$ contradict inequality. □

Therefore, the external potential $v_{ext}(\mathbf{r})$ is determined by the ground state density uniquely, except only for the sum of constant. The distribution of electrons affect the positions of the nucleus of an atom. In addition, they determine all physical properties of ground state because Hamiltonian $\hat{H}$ is defined by external potential $v_{ext}(\mathbf{r})$ and number of electrons N. The total energy functional $E[n(\mathbf{r})]$ can be represented by means of the external potential $v_{ext}(\mathbf{r})$ as follows,

$$E[n(\mathbf{r})] = \int n(\mathbf{r})v_{ext}(r)d\mathbf{r} + F[n(\mathbf{r})] \tag{2.4}$$

where $F[n(\mathbf{r})]$ is an unidentified and universal functional. Ground state energy functional is expressed by Hamiltonian expectation value $\hat{H}$ for the wavefuntion $|\Psi\rangle$ minimizing the total energy of the system. Ground state energy functional and Hamiltonian can be described as follows,

$$E[n(\mathbf{r})] = \langle\Psi|\hat{H}|\Psi\rangle, \tag{2.5}$$

$$\hat{H} = \hat{F} + \hat{V}_{ext}, \tag{2.6}$$

respectively. $\hat{F}$ is equal for all systems with electron number N. Therefore, $\hat{H}$ is determined by the external potential $v_{ext}(\mathbf{r})$ and electron numbers N.

Theorem 2 *When the ground state density is entered to energy functional, total energy has minimum value. Therefore, one can obtain the ground state energy by using variational principles.*

Proof. External potential $v_{ext}(\mathbf{r})$ is determined by electron density $n(\mathbf{r})$. In addition, Hamiltonian $\hat{H}$ and wavefunction Ψ of system are determined by external potential $v_{ext}(\mathbf{r})$ and number of electrons N. Expectation value of universal function $\hat{F}$ in Eq. (2.6) is functional of $n(\mathbf{r})$ because Ψ is functional of $n(\mathbf{r})$.

$$F[n(\mathbf{r})] = \langle \Psi | \hat{F} | \Psi \rangle \tag{2.7}$$

The ground state density can be characterized by certain external potential v. Therefore, energy functional $E_v[n'(\mathbf{r})]$ is defined by external potential $v_{ext}(\mathbf{r})$ and electron density $n'(\mathbf{r})$ which is different from ground state density,

$$E_v[n'(\mathbf{r})] = \int n'(\mathbf{r}) v_{ext}(\mathbf{r}) d\mathbf{r} + F[n'(\mathbf{r})]. \tag{2.8}$$

Using variational priciples,

$$\langle \Psi' | \hat{F} | \Psi' \rangle + \langle \Psi' | \hat{V}_{ext} | \Psi' \rangle > \langle \Psi | \hat{F} | \Psi \rangle + \langle \Psi | \hat{V}_{ext} | \Psi \rangle \tag{2.9}$$

where Ψ is the wavefunction corresponds to the exact ground state electron density $n(\mathbf{r})$. It gives following result

$$\int n'(\mathbf{r}) v_{ext}(\mathbf{r}) d\mathbf{r} + F[n'(\mathbf{r})] > \int n(\mathbf{r}) v_{ext}(\mathbf{r}) d\mathbf{r} + F[n(\mathbf{r})], \tag{2.10}$$

which is the second Hohenberg-Kohn theorem,

$$E_v[n'(\mathbf{r})] > E_v[n(\mathbf{r})]. \tag{2.11}$$

□

2.1.2 Kohn-Sham Equation

Hohenberg-Kohn theorem shows properties such as the external potential and total energy of ground state are determined and can be evaluated using electron density. However, it does not provide a specific solution of calculating the ground state electron density. Kohn-Sham equation gives practical solution of ground state electron density by replacing the N-particle problem to single-particle problem.[35] To be specific, systems with interacting particles under the real potential are substituted by non-interacting particles system under an effective single-particle potential $v_{KS}(\mathbf{r})$, called Kohn-Sham potential. Again, ground state energy can be estimanted by minimizing energy functional of many-body systems (variational principle). The constraint of electron numbers N conservation gives

$$\delta\left[F[n(\mathbf{r})] + \int v_{ext}(\mathbf{r})n(\mathbf{r})d\mathbf{r} - \mu\left(\int n(\mathbf{r})d\mathbf{r} - N\right)\right] = 0 \tag{2.12}$$

and the Lagrange multiplier μ can be written by

$$\mu = \frac{\delta F[n(\mathbf{r})]}{\delta n(\mathbf{r})} + v_{ext}(\mathbf{r}). \tag{2.13}$$

The ground state wave function Ψ_{KS} (Kohn-Sham wavefunction) can be represented by a determinant of matrix as following equation where the components $\psi_i(\mathbf{r}_i)$ is single-particle orbitals.

$$\Psi_{KS} = \frac{1}{\sqrt{N!}} det[\psi_1(\mathbf{r}_1)\psi_2(\mathbf{r}_2)...\psi_N(\mathbf{r}_N)]. \tag{2.14}$$

The universal functional $F[n(\mathbf{r})]$ in Eq. (2.12) can be divided by three parts,

$$F[n(\mathbf{r})] = T_S[n(\mathbf{r})] + E_H[n(\mathbf{r})] + E_{XC}[n(\mathbf{r})]. \tag{2.15}$$

First term $T_S[n(\mathbf{r})]$ is the kinetic energy functional of a non-interacting particle with electron density $n(\mathbf{r})$. Second term $E_H[n(\mathbf{r})]$ corresponds to electrostatic energy functional written as,

$$E_H[n(\mathbf{r})] = \frac{1}{2}\int\int \frac{n(\mathbf{r})n(\mathbf{r}')}{|\mathbf{r}-\mathbf{r}'|}d\mathbf{r}d\mathbf{r}'. \tag{2.16}$$

Final term $E_{XC}[n(\mathbf{r})]$ is known as the exchange-correlation energy functional. This term is divided by exchange and correlation terms, each of them containing repulsion among the electrons with same spin component and Coulomb repulsion, respectively. Using Eq. (2.15) into Eq. (2.13), Lagrange multiplier μ becomes

$$\mu = \frac{\delta T_S[n(\mathbf{r})]}{\delta n(\mathbf{r})} + v_{KS}(\mathbf{r}), \tag{2.17}$$

where $v_{KS}(\mathbf{r})$ is written as,

$$v_{KS}(\mathbf{r}) = v_{ext}(\mathbf{r}) + v_H(\mathbf{r}) + v_{XC}(\mathbf{r}). \tag{2.18}$$

Second and third term in Eq. (2.18) corresponds to the Hartree potential and the exchange-correlation potential which is given by,

$$v_H(\mathbf{r}) = \frac{\delta E_H[n(\mathbf{r})]}{\delta n(\mathbf{r})} = \int \frac{n(\mathbf{r}')}{|\mathbf{r}-\mathbf{r}'|}d\mathbf{r}' \tag{2.19}$$

and

$$v_{XC}(\mathbf{r}) = \frac{\delta E_{XC}[n(\mathbf{r})]}{\delta n(\mathbf{r})}, \tag{2.20}$$

respectively. The wave function and density of ground state can be estimated by calculating the N number of following single-particle Schrodinger equations

$$\left[-\frac{1}{2}\nabla^2 + v_{KS}(\mathbf{r})\right]\psi_i(\mathbf{r}) = \varepsilon_i\psi_i(\mathbf{r}), \tag{2.21}$$

Using the single-particle wave function $\psi_i(\mathbf{r})$, the electron density is defined as,

$$n(\mathbf{r}) = \sum_{i=1}^{N} |\psi_i(\mathbf{r})|^2. \tag{2.22}$$

Kohn-Sham potential $v_{KS}(\mathbf{r})$ has a dependence of electron density $n(\mathbf{r})$ because of the exchange-correlation part $v_{XC}(\mathbf{r})$. Therefore, one can obtain converged electron density by solving the Kohn-Sham equation self-consistently. Remaining task is to determine the specific form of exchange-correlation energy functional $E_{XC}[n(\mathbf{r})]$. In the following sections, approximations of exchange-correlation energy functional are introduced that constructing functional as a function of only electron density or together with gradient of electron density.

2.1.3 Local Density Approximation

The basic approach for the exchange-correlation energy functional is so called local density approximation (LDA). This approximation is considering exchange-correlation energy functional depends notably on the spatial distribution of the electron density in real space. The exchange-correlation energy functional for LDA is given by,

$$E_{XC}^{LDA}[n(\mathbf{r})] = \int n(\mathbf{r}) \varepsilon_{XC}[n(\mathbf{r})] d\mathbf{r}, \tag{2.23}$$

where ε_{XC} is the exchange-correlation energy functional per particle of a homogeneous electron gas (HEG). The exchange-correlation energy functional can be divided by exchange and correlation parts, $E_{XC}^{LDA}[n(\mathbf{r})] = E_{X}^{LDA}[n(\mathbf{r})] + E_{C}^{LDA}[n(\mathbf{r})]$. The exchange energy functional part has an analytic form as follows,

$$E_{X}^{LDA}[n(\mathbf{r})] = -\frac{3}{4}\left(\frac{3}{\pi}\right)^{1/3} \int n(\mathbf{r})^{4/3} d\mathbf{r}. \tag{2.24}$$

The correlation energy functional part is also represented by analytic expressions decomposed by the high and low density limits written as,

$$E_C^{LDA}[n(\mathbf{r})] = \begin{cases} A\ln(r_s) + B + r_s(C\ln(r_s) + D), & \text{if } r_s < 1 \\ \frac{\gamma}{1+\beta_1\sqrt{(r_s)}+\beta_2 r_s}, & \text{if } r_s > 1 \end{cases} \tag{2.25}$$

where $r_s(n(\mathbf{r})) = (\frac{3}{4\pi n(\mathbf{r})})^{1/3}$. The coefficients in Eq. (2.25) are A = 0.0311, B = -0.048, C = 0.002, D = -0.0116, γ = -0.1423 , β_1 = 1.0529 and β_2 = 0.3334, respectively in Hartree unit which is given by the most accurate result in parameterized by Perduw and Zunger[36] based on the quantum Monte Carlo simulations for HEG[37].

2.1.4 Generalized Gradient Approximation

In previous section, we discussed about LDA which assumes the slowly varying electron density. However, the electron density of system undergoes rapid variations, the approximation is not valid anymore. Therefore, the non-local effect of electron density on energy functional should be considered. Generalized Gradient Approximation (GGA) is a way of considering non-locality via taking into account gradient of electron density in exchange-correlation energy functional.

$$E_{XC}^{GGA} = E_{XC}^{GGA}[n(\mathbf{r}), \nabla n(\mathbf{r})] \tag{2.26}$$

The representative form of GGA exchange-correlation energy functional is the one proposed by Perdew, Burke and Ernzerhof[38], so called PBE functional. It can be written as,

$$E_{XC}^{GGA}[n(\mathbf{r})] = \int n(\mathbf{r})\varepsilon_X[n(\mathbf{r})]F_{XC}(r_s, \zeta, s)d\mathbf{r} \tag{2.27}$$

where F_{XC} is enhancement factor, ζ is relative spin polarization and s is dimensionless spatial gradient of electron density written as s=$\frac{|\nabla n(\mathbf{r})|}{2k_F n(\mathbf{r})}$.

2.2 DFT+U Calculation

So far, we discuss exchange-correlation functional with relevant approximations. However, there is drawback in treating exchange-correlation functional in DFT calculation that it does not estimate self-interaction effect precisely which is significant for strongly correlated system. The DFT+U method can be a solution of such problems by considering effect of on-site Coulomb repulsion in single-particle pictures[39]. In DFT+U calculation, generalized Hubbard model[40, 41] is combined with simple DFT calculation where double counting term is corrected. The total energy functional is given by

$$\begin{aligned} E_{DFT+U}[n(\mathbf{r})] &= E_{DFT}[n(\mathbf{r})] + E_{Hub}[\{n^{I\sigma}_{mm'}\}] - E_{DC}[\{n^{I\sigma}\}] \\ &= E_{DFT}[n(\mathbf{r})] + E_{U}[\{n^{I\sigma}_{mm'}\}], \end{aligned} \tag{2.28}$$

where $n(\mathbf{r})$ and $n^{I\sigma}_{mm'}$ corresponds to electron density and the orbital occupation of I-th atom with spin σ and angular momentum m, respectively[42]. The double counting term $E_{DC}[\{n^{I\sigma}\}]$ is a function of net orbital occupation $n^{I\sigma} = \sum_m n^{I\sigma}_{mm}$ which is distinct from Hubbard term $E_{Hub}[\{n^{I\sigma}_{mm'}\}]$ as a function of $n^{I\sigma}_{mm'}$[39, 43, 44]. The orbital occupation $n^{I\sigma}_{mm'}$ is represented by projection of electron wavefunction $|\psi^{\sigma}_{k}\rangle$ onto orbital $|\phi^{I}_{m}\rangle$

$$n^{I\sigma}_{mm'} = \sum_k f_k \langle \psi^{\sigma}_{k} | \phi^{I}_{m'} \rangle \langle \phi^{I}_{m} | \psi^{\sigma}_{k} \rangle, \tag{2.29}$$

where $\mathbf{k}$ is wavevector and f_k is the weight of the k-th electronic state. General form of $E_U[\{n^{I\sigma}_{mm'}\}]$ is given by introducing formalism of Dudarev et al. which

choose unrestricted Hartree-Fock(UHF) description of one electonic states[45]. In this formalism, $E_{U_{eff}}[\{n^{I\sigma}_{mm'}\}]$ depends on $U_{eff} = U - J$ where U and J is the on-site Coulomb interaction term and exchange parameter, respectively. The energy functional is given by,

$$\begin{aligned} E_{U_{eff}}[\{n^{I\sigma}_{mm'}\}] &= \frac{U_{eff}}{2} \sum_{I} \sum_{m,\sigma} \left[n^{I\sigma}_{mm} - \sum_{m'} n^{I\sigma}_{mm'} n^{I\sigma}_{m'm} \right] \\ &= \frac{U_{eff}}{2} \sum_{I\sigma} Tr[\hat{n}^{I\sigma}(1 - \hat{n}^{I\sigma})]. \end{aligned} \tag{2.30}$$

By diagonalizing the occupation matrices $\hat{n}^{I\sigma}$, Eq. (2.30) can be rewritten as follows

$$E_U[\{n^{I\sigma}_{mm'}\}] = \frac{U}{2} \sum_{I\sigma} \sum_{i} \lambda^{I\sigma}_i (1 - \lambda^{I\sigma}_i), \tag{2.31}$$

where $\lambda^{I\sigma}_i$ is electronic occupation of I-th atomic orbital. When U_{eff} value is positive, occupation $\lambda^{I\sigma}_i$ should be 0 or 1 so that $E_U[\{n^{I\sigma}_{mm'}\}]$ vanishes for minimizing energy functional. It implies that situations of unoccupied ($\lambda^{I\sigma}_i = 0$) or fully occupied ($\lambda^{I\sigma}_i = 1$) orbitals are favored which corrects over-estimation of the self-interactions in partially filled orbitals.

2.3 Spin-orbit Coupling within Non-collinear Spin Formalism

2.3.1 Non-collinear Spin Density Functional

A wavefunction with two-component spinor is defined by

$$|\psi_\nu\rangle = |\varphi^\alpha_\nu \alpha\rangle + |\varphi^\beta_\nu \beta\rangle, \tag{2.32}$$

where $|\varphi_\nu^\alpha \alpha\rangle \equiv |\varphi_\nu^\alpha\rangle|\alpha\rangle$ with a spatial part $|\varphi_\nu^\alpha\rangle$ and a spin part $|\alpha\rangle$. Then, the density operator can be written by

$$\hat{n} = \sum_\nu f_\nu |\phi_n u\rangle\langle\phi_\nu| = \sum_\nu f_\nu \big(|\varphi_\nu^\alpha \alpha\rangle + |\varphi_\nu^\beta \beta\rangle\big)\big(\langle\varphi_\nu^\alpha \alpha| + \langle\varphi_\nu^\beta \beta|\big), \tag{2.33}$$

where f_ν should be a step function. With the definition of density operator $\hat{n}$, a non-collinear electronic density in real space is represented as

$$n_{\sigma\sigma'} = \langle \mathbf{r}\sigma|\hat{n}|\mathbf{r}\sigma'\rangle = \sum_\nu f_\nu \varphi_\nu^\sigma \varphi_\nu^{\sigma'*}, \tag{2.34}$$

where σ, σ' is spin indices α or β and $|\mathbf{r}\rangle$ is a position eigenvector. The $n'_\uparrow$ (up-spin density) and $n'_\downarrow$ (down-spin density) at each point are defined by diagonalizing non-collinear electronic densities matrix as follows:

$$\begin{pmatrix} n'_\uparrow & 0 \\ 0 & n'_\downarrow \end{pmatrix} = UnU^\dagger = U \begin{pmatrix} n_{\alpha\alpha} & n_{\alpha\beta} \\ n_{\beta\alpha} & n_{\beta\beta} \end{pmatrix} U^\dagger \tag{2.35}$$

The total energy of non-collinear functional[46, 47] could be written by

$$\begin{aligned} E_{tot} = &\sum_{\sigma=\alpha,\beta}\sum_\nu f_\nu \langle\varphi_\nu^\sigma|\hat{T}|\varphi_\nu^\sigma\rangle + \sum_{\sigma\sigma'}\int w_{\sigma\sigma'}(\mathbf{r}) n_{\sigma'\sigma}(\mathbf{r}) d\mathbf{r} \\ &+ \frac{1}{2}\int\int \frac{n'(\mathbf{r})n'(\mathbf{r}')}{|\mathbf{r}-\mathbf{r}'|} d\mathbf{r}d\mathbf{r}' + E_{XC}\{n_{\sigma\sigma'}\}, \end{aligned} \tag{2.36}$$

where the first, second, third and fourth term corresponds to the kinetic energy, Coulomb interaction of core electrons, electron-electron Coulomb energy and exchange-correlation energy functional, respectively. The total energy can also be represented in terms of the Kohn-Sham eigen-energies ε_ν as follows:

$$E_{tot} = E_{band} - \frac{1}{2}\int n' V_H d\mathbf{r} - \int Tr(V_{XC} n) d\mathbf{r} + E_{XC}, \tag{2.37}$$

where V_{XC} is a non-collinear exchange-correlation potential functional. By using orthogonality relation of spinor wavefunctions, a functional F is introduced:

$$F = E_{tot} + \sum_{\nu\nu'} \varepsilon_{\nu\nu'}(\delta_{\nu\nu'} - \langle\psi_\nu|\psi_{\nu'}\rangle). \tag{2.38}$$

The variation of F with respect to φ is presented by

$$\frac{\delta F}{\delta\varphi_\mu^{\sigma,*}} = \hat{T}\varphi_\mu^\sigma + \sum_{\sigma'} w_{\sigma\sigma'}\varphi_\mu^{\sigma'} + V_H\varphi_\mu^\sigma + \sum_{\sigma'} V_{XC}^{\sigma\sigma'}\varphi_\mu^{\sigma'} - \sum_\nu \varepsilon_{\mu\nu}\varphi_\nu^\sigma \tag{2.39}$$

with

$$V_H = \int \frac{n'(\mathbf{r}')}{|\mathbf{r} - \mathbf{r}'|} d\mathbf{r}, V_{XC}^{\sigma\sigma'} = \frac{\delta E_{XC}}{\delta n_{\sigma'\sigma}}. \tag{2.40}$$

The variation of F in Eq. (2.39) to be zero with diagonalizing $\varepsilon_{\mu\nu}$ for unitary transform φ_ν^σ, the non-collinear Kohn-Sham equation can be obtained,

$$\begin{pmatrix} \hat{T} + w_{\alpha\alpha} + V_H + V_{XC}^{\alpha\alpha} & w_{\alpha\beta} + V_{XC}^{\alpha\beta} \\ w_{\beta\alpha} + V_{XC}^{\beta\alpha} & \hat{T} + w_{\beta\beta} + V_H + V_{XC}^{\beta\beta} \end{pmatrix} \begin{pmatrix} \varphi_\mu^\alpha \\ \varphi_\mu^\beta \end{pmatrix} = \varepsilon_\mu \begin{pmatrix} \varphi_\mu^\alpha \\ \varphi_\mu^\beta \end{pmatrix}. \tag{2.41}$$

The off-diagonal term in Eq. (2.41) contains exchange-correlation functional and another contribution w such as spin-orbit coupling effect between spin component α and β. In Eq. (2.35), the unitary transformation U diagonalize the average non-collinear spin density matrix. If we diagonalize this non-collinear spin density matrix n, we can calculate the exchange-correlation functional $\bar{V}_{XC}$ using the diagonal term for up- and down- spin densities based on LDA or GGA formalism. The $\bar{V}_{XC}$ is given by

$$\begin{aligned} \bar{V}_{XC} &= \begin{pmatrix} V_{XC}^\uparrow & 0 \\ 0 & V_{XC}^\downarrow \end{pmatrix} \\ &= \frac{1}{2}(V_{XC}^\uparrow + V_{XC}^\downarrow)\mathbf{I} + \frac{1}{2}(V_{XC}^\uparrow - V_{XC}^\downarrow)\sigma_3 \end{aligned}$$

$$= V^0_{XC}\mathbf{I} + \triangle V_{XC}\sigma_3, \tag{2.42}$$

where σ_3 is third matrix of Pauli matrices. The non-collinear exchange-correlation V_{XC} is unitary transformation U of $\bar{V}_{XC}$,

$$\begin{aligned} V_{XC} &= U^\dagger \bar{V}_{XC} U \\ &= V^0_{XC}\mathbf{I} + \triangle V_{XC} U^\dagger \sigma_3 U \\ &= V^0_{XC}\mathbf{I} + \triangle V_{XC}\bar{\sigma}_3 \end{aligned} \tag{2.43}$$

Finally, the effective potential V_{eff} can be represented by Pauli matrices,

$$V_{eff} = V^0_{eff}\sigma_{\mathbf{0}} + \triangle V_{XC}\bar{\sigma}_3 + w \tag{2.44}$$

where

$$V^0_{eff} = V_H + V^0_{XC}, w = \begin{pmatrix} w_{\alpha\alpha} & w_{\alpha\beta} \\ w_{\beta\alpha} & w_{\beta\beta} \end{pmatrix}. \tag{2.45}$$

2.3.2 Spin-orbit Coupling

The spin-orbit coupling effect is implemented as j-dependent pseudo potentials in OpenMX code mainly used in our research. Radial part of coupled Dirac equations in spherical symmetric system is givne by

$$\begin{aligned} \frac{dG_{nlj}}{dr} + \frac{\kappa}{r}G_{nlj} - a\left[\frac{2}{a^2} + \varepsilon_{nlj} - V(r)\right]F_{nlj} = 0 \\ \frac{dF_{nlj}}{dr} - \frac{\kappa}{r}F_{nlj} + a[\varepsilon_{nlj} - V(r)]G_{nlj} = 0, \end{aligned} \tag{2.46}$$

where G and F are the majority and minority components of the radial wave function, $a \equiv 1/137 in a.u.$, $\kappa = l$ and $\kappa = -(l+1)$ for $j = l-1/2$ and $j = l+1/2$, respectively. Collecting two equations in Eq. (2.46) for erasing F, one can get

following equation for G:

$$\left[\frac{1}{2M(r)}\left(\frac{d^2}{dr^2}+\frac{a^2}{2M(r)}\frac{dV}{dr}\frac{d}{dr}+\frac{a^2}{2M(r)}\frac{\kappa}{r}\frac{dV}{dr}-\frac{\kappa(\kappa+1)}{r^2}\right)+\varepsilon_{nlj}-V\right]G_{nlj}=0 \tag{2.47}$$

with

$$M(r)=1+\frac{a^2(\varepsilon_{nlj}-V)}{2}. \tag{2.48}$$

By numerical solving of Eq. (2.47) and generating j-dependent pseudopotential V_j^{ps}, one can define a general pseudopotential,

$$V_{ps}=\sum_{lm}\Big[|\Phi_J^M\rangle V_{ps}^{l+1/2}\langle\Phi_J^M|+|\Phi_{J'}^{M'}\rangle V_{ps}^{l-1/2}\langle\Phi_{J'}^{M'}|\Big], \tag{2.49}$$

where for $J=l+1/2$, $M=m+1/2$

$$|\Phi_J^M\rangle=\Big(\frac{l+m+1}{2l+1}\Big)^{1/2}|Y_l^m\rangle|\alpha\rangle+\Big(\frac{l-m}{2l+1}\Big)^{1/2}|Y_l^{m+1}\rangle|\beta\rangle, \tag{2.50}$$

and for $J'=l-1/2$, $M'=m-1/2$

$$|\Phi_{J'}^{M'}\rangle=\Big(\frac{l-m+1}{2l+1}\Big)^{1/2}|Y_l^{m-1}\rangle|\alpha\rangle-\Big(\frac{l+m}{2l+1}\Big)^{1/2}|Y_l^m\rangle|\beta\rangle. \tag{2.51}$$

Φ_J^M and $\Phi_{J'}^{M'}$ are elements of eigenfunctions for Dirac equations. If we introduce a local potential V_L which close to $-\frac{Z_{eff}}{r}$ as r increases, the j-dependent pseudopotential is divided into two components,

$$\begin{aligned}V_{ps}^{l+1/2}&=V_{NL}^{l+1/2}+V_L\\ V_{ps}^{l-1/2}&=V_{NL}^{l-1/2}+V_L.\end{aligned} \tag{2.52}$$

Finally, pseudopotential in Eq. (2.49) is given by

$$\begin{aligned}V_{ps}&=V_L+\sum_{lm}\left[|\Phi_J^M\rangle V_{NL}^{l+1/2}\langle\Phi_J^M|+|\Phi_{J'}^{M'}\rangle V_{NL}^{l-1/2}\langle\Phi_{J'}^{M'}|\right]\\ &=V_L+\bar{V}_{NL}^{l+1/2}+\bar{V}_{NL}^{l-1/2}\end{aligned} \tag{2.53}$$

The non-local potential term is transformed by the Bloch projector into a separable form.

2.4 Maximally Localized Wannier Functions

According to Bloch theorem, electronic state under periodic potentials has a form of plane wave modulated by periodic function,

$$|\psi_{n\mathbf{k}}(\mathbf{r})\rangle = e^{i\mathbf{k}\cdot\mathbf{r}}|u_{n\mathbf{k}}\rangle \tag{2.54}$$

where $u_{n\mathbf{k}}$ is periodic function, n is band index, $\mathbf{k}$ and $\mathbf{r}$ is crystal momentum and position vector, respectively. By using Fourier transformation of this electronic state, it can be represented in real space generating Wannier function (WF)[48],

$$|\mathbf{R}n\rangle = \frac{V}{(2\pi)^3}\int_{BZ} d\mathbf{k} e^{i\mathbf{k}\cdot\mathbf{R}}|\psi_{n\mathbf{k}}(\mathbf{r})\rangle \tag{2.55}$$

where the integral is carried out over the Brillouin zone (BZ). $\mathbf{R}$ and V is real space lattice vector and volume of real space primitive cell. However, there exist gauge freedom in the theory of WF. One can substitute

$$|\tilde{\psi}_{n\mathbf{k}}\rangle = e^{i\varphi_n(\mathbf{k})}|\psi_{n\mathbf{k}}\rangle \tag{2.56}$$

without any change of physical properties, where $\varphi_n(\mathbf{k})$ is arbitrary real and periodic function in momentum space. In multiband case with J bands manifold, Bloch orbitals are given by gauge transformation

$$|\tilde{\psi}_{n\mathbf{k}}\rangle = \sum_{m=1}^{J} U_{mn}^{(\mathbf{k})}|\psi_{m\mathbf{k}}\rangle. \tag{2.57}$$

$U_{mn}^{(\mathbf{k})}$ is a J dimension unitary matrix which mixes the Bloch orbitals at each $\mathbf{k}$ points. The resulting WF is written as,

$$|\mathbf{R}n\rangle = \frac{V}{(2\pi)^3}\int_{BZ} d\mathbf{k} e^{i\mathbf{k}\cdot\mathbf{R}} \sum_{m=1}^{J} U_{mn}^{(\mathbf{k})} |\psi_{m\mathbf{k}}\rangle. \tag{2.58}$$

Therefore, it is remaining task to know how to choose unitary matrix $U_{mn}^{(\mathbf{k})}$. The method of finding unique $U_{mn}^{(\mathbf{k})}$ is developed by maximizing localization of WF[49]. Spread functional which describes the quantity of spatial spread of WF is defined as follows,

$$\Omega = \sum_n \left[\langle \mathbf{0}n|r^2|\mathbf{0}n\rangle - \langle \mathbf{0}n|r|\mathbf{0}n\rangle^2\right] = \sum_n \left[\langle r^2\rangle_n - \bar{\mathbf{r}}_n^2\right]. \tag{2.59}$$

By minimizing the gauge dependent part of spread function, the unitary transformation $U_{mn}^{(\mathbf{k})}$ is determined so that the maximally localized Wannier function(MLWF) can be obtained.

Chapter 3

Effect of Coulomb Interactions on the Electronic and Magnetic Properties of Two-Dimensional $CrSiTe_3$ and $CrGeTe_3$ Materials

In this chapter, we introduce one of our main research of electronic and magnetic properties of $CrSiTe_3$ and $CrGeTe_3$ compounds[50]. First, we find electronic and structural ground state by performing total energy and structure optimization calculations. Then, we investigate the effect of Coulomb interaction in magnetism and band gap energy by changing the Hubbard U parameters. We suggest relevant Hubbard U value which gives comparable results with experiment and reasonable magnetic ground state.

3.1 Introduction

Transition metal di-chalcogenides (TMDC) in their atomically thin two-dimensional (2d) forms exhibit a wide range of electronic, optical, mechanical, chemical and

thermal properties. In particular, their tunable bandgap properties depending on the number of layers make this class of materials as a candidate for future electronics and optoelectronics applications[4, 5]. Due to the presence of transition metal atoms, however, the emergence of magnetism in 2d crystals has opened up interesting possibilities. For example, chromium tri-iodide (CrI_3) was suggested as an ideal candidate for 2d magnets exfoliated from easily cleavable single crystals of CrI_3, which is a layered and insulating ferromagnet with a Curie temperature of 61 K[51]. A recent observation of ferromagnetism has demonstrated its layer dependence down to the monolayer limit[12]. Along with TMDC, another class of layered transition-metal tri-chalcogenides (TMTC) with the chemical formula ABX_3 (A = Mn, Cr; B= Si, Ge; X = S, Se, Te) have attracted interest as potential candidates for 2d magnets[6]. Although these ABX_3-class of TMTC materials have been studied for many decades [51–57], their electronic and magnetic structures as well as mechanism for magnetic ordering are not clearly understood yet. For instance, $CrSiTe_3$, one of the TMTC materials, is well known as a candidate for a 2d ferromagnetic (FM) semiconductor. The Curie temperatures were reported to increase as the number of layers is reduced[32, 33]. On the other hand, however, there is controversy of predicting magnetic ground states of $CrSiTe_3$ monolayer[6, 31]. Further, a magnetic phase transition can be induced by the tensile strain in $CrSiTe_3$ monolayer[6, 31]. Despite ferromagnetism and insulating properties are reported in bulk structure of $CrSiTe_3$[58], observing monolayer structure of $CrSiTe_3$ has never been realized. Therefore, it is crucial to demonstrate electronic and magnetic properties of $CrSiTe_3$ monolayer. As a step toward understanding the origin of ferromagnetism in the ABX_3-class materials, we investigate the electronic and magnetic structures of 2d TMTC $CrSiTe_3$ and

$CrGeTe_3$ materials by carrying out first-principles calculations. We performed total energy calculations for various magnetic configurations in single-, bi-, and triple-layers as well as bulk $CrSiTe_3$ and $CrGeTe_3$ including their full structural optimizations. We also examine the effect of on-site Coulomb interactions U for Cr d electrons by monitoring the bandgap and magnetic order. The results show an unusual behavior of bandgap as well as magnetic order depending on U, which may provide a clue to the understanding of the electronic and magnetic properties of the ABX_3-type TMTC materials in general.

3.2 Computational Details

The first-principles calculations were performed by using density-functional theory (DFT) within the generalized gradient approximation GGA+U method. To obtain band structures and projected density-of-states (pDOS), we use the OpenMX code[59, 60] which employ localized orbital bases, especially with the GGA exchange-correlation functional in the parameterization of Perdew, Burke and Enzerhof (PBE)[38]. We use the effective on-site Coulomb interaction $U_{\text{eff}} = U - J$ in a Dudarev implementation[45, 61] to treat the localized Cr d states throughout the calculations. We examine the electronic and magnetic structures by varying the U_{eff} values from 0.0 to 3.0 eV, which will be called as U from now on, for simplicity. The non-collinear DFT calculations are performed with the spin-orbit coupling (SOC) incorporated through the fully relativistic j-dependent pseudo potentials as implemented in the OpenMX code. To simulate a single or few layers of 2d $CrBTe_3$ (B = Si, Ge) systems, we make use of a slab geometry with 20 Å vacuum in-between the layers, where each layer consists of a 2d honeycomb lattice with the $Cr_2B_2Te_6$ unit cell. The

cutoff energy of 500 Ry is used for the real and momentum space grids and the **k**-mesh of $10 \times 10 \times 1$ for the Brillouin zone integration. The lattice structures are relaxed under the contraint of C_3 rotation symmetry until the residual forces converge within 10^{-4} in atomic unit.

3.3 Results and Discussion

3.3.1 Electronic Structure and Magnetic Properties of Single-layer $CrSiTe_3$

We carried out first-principles calculations for the ground states of $CrBTe_3$ (B = Si, Ge). Our results of the electronic band structures and the magnetic ground states for the single layer and bulk systems are in general agreement with the previous works[6, 8, 31, 32, 58]. To calculate the electronic band structures and pDOS, we adopt the on-site Coulomb interaction parameter of $U = 1.5$ eV. More discussion one the choice of U will be made in Sec. 3.3.2. Both single-layer $CrSiTe_3$ and $CrGeTe_3$ are determined to be a FM insulator. Bulk structure of $CrSiTe_3$ and $CrGeTe_3$ have the same space group of $R\overline{3}$ (No.148) in common with other ABX_3 type TMTC. The optimized in-plane lattice constant slightly depends on the choice of Hubbard U, it is calculated as $a = 6.88$ Å for $CrSiTe_3$ and $a = 6.95$ Å for $CrGeTe_3$ monolayer, respectively when $U = 1.5$ eV. Crystal structure of $CrSiTe_3$ monolayer is depicted in Fig. 3.1. Basically, Cr atoms are consisting honeycomb lattice where Si atoms are located at the center of honeycomb with dimerized structure. Each Cr atom is surrounded by six Te atoms consisting $CrTe_6$ octahedron, where it is slightly distorted due to trigonal distorted under relaxed structure. Each $CrTe_6$ octahedron shares its

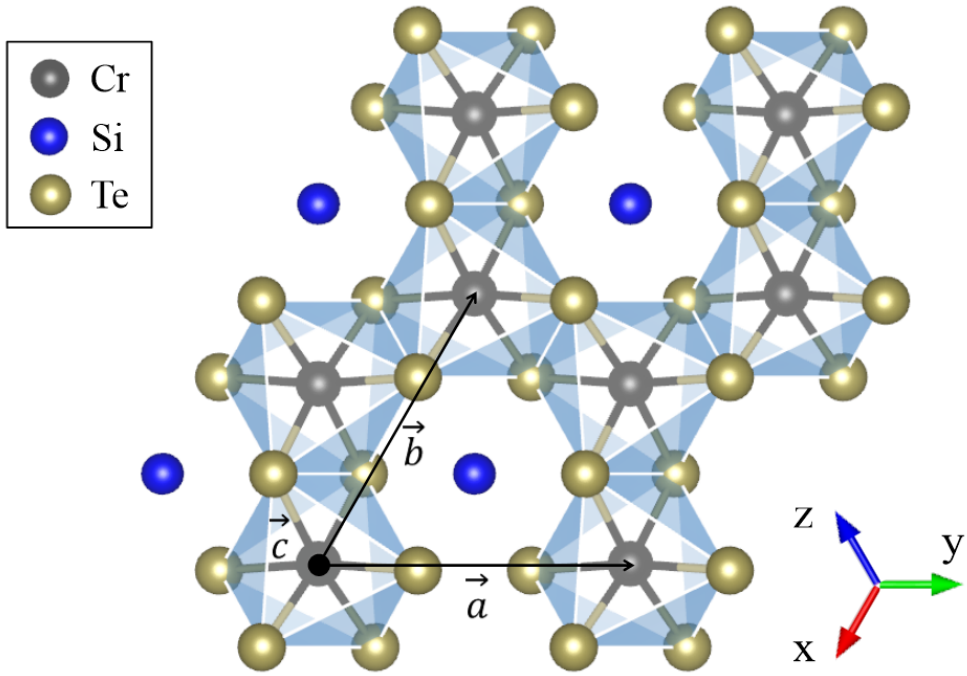

Figure 3.1 (Color online) Top view of monolayer $CrSiTe_3$ crystal structure. Edge sharing $CrTe_6$ octahedron consists of Cr atom (black sphere) and surrounding six Te atoms (yellow sphere). Dimerized two Si atoms (blue sphere) are sitting at center of Cr honeycomb lattice. **a**,**b**,**c** is unit vector of hexagonal unit cell, where **x**,**y**,**z** indicates local axis.

edge with adjacent $CrTe_6$ octahedrons. Under octahedral environment, Cr d orbitals are split into three t_{2g} levels with lower energy and two e_g levels with higher energy eigenstates. In $CrSiTe_3$ and $CrGeTe_3$ compounds, Cr d orbital has $3d^3$ occupation so that electrons are occupying three t_{2g} levels with up-spin states, i.e. high spin states.

This characteristics are described in Fig. 3.2 which shows the spin-polarized band structure and pDOS for the FM single-layer $CrSiTe_3$ with $U = 1.5$ eV. Since $CrGeTe_3$ exhibits similar features of the valence and conduction bands except for the states related to Ge, here we focus on the electronic structure of $CrSiTe_3$ only. The prominent features of the $CrSiTe_3$ electronic structure

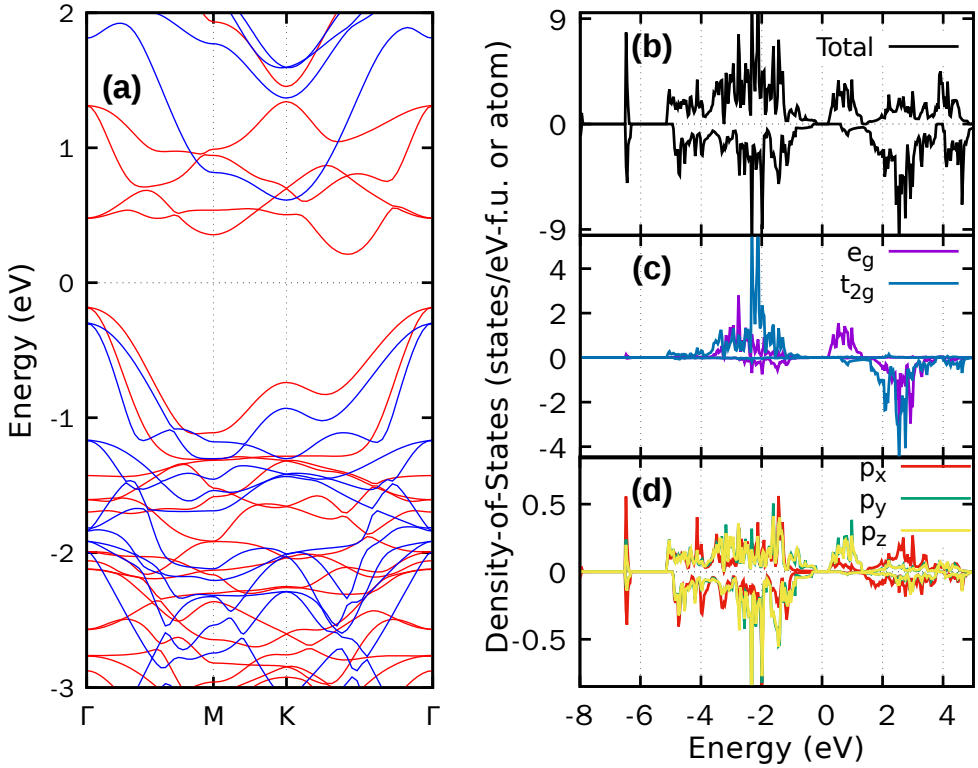

Figure 3.2 (Color online) (a) Band structure, (b) total, (c) Cr- and (d) Te-pDOS of ferromagnetic single-layer $CrSiTe_3$ at $U = 1.5$ eV. In the band structure plot, the majority-spin (minority spin) bands are marked by the red (blue) lines, respectively. In the pDOS plots, the upper panel represents for the majority-spin (spin-up) components of the pDOS and the lower panel for the minority (spin-down) components, where the Fermi level (E_F) is set to zero.

are the empty $dp\sigma$-hybridized anti-bonding bands of Cr e_g - Te p at 1 eV above the Fermi level (E_F) and the fully occupied Cr $t_{2g}^{3\uparrow}$ bands at about -2 eV below E_F. Bandgap energy is constructed between Cr e_g bands and Te p bands. The unoccupied spin-down (minority-spin) bands of Cr t_{2g} are located at about 2 eV above E_F, indicating a large exchange splitting of the localized Cr t_{2g} orbitals.

Thus, the local magnetic moment of each Cr atom is 3.87 μ_B, where the extra contribution of 0.87 μ_B comes from the $dp\sigma$ bonding states of Cr e_g

- Te p. In fact, this Cr - Te $dp\sigma$ hybridization gives rise to the Te p holes with a opposite spin polarization of -0.3 μ_{B} per Te atom so that the total FM moment per $CrSiTe_3$ unit-cell remains 3 μ_{B}. In addition, the single-ion anisotropy energy is found to be about 0.77 meV and 0.31 meV per Cr atom with an easy axis perpendicular to the layer for the single-layer $CrSiTe_3$ and $CrGeTe_3$, respectively. It indicates that both $CrSiTe_3$ and $CrGeTe_3$ are Ising-like ferromagnets, in agreement with previous experiments[58] and calculation results[62].

The origin of ferromagnetism can be explained by GKA rules(super-exchange mechanisms)[63, 64]. Fig. 3.3 shows super-exchange hopping process in $CrSiTe_3$. In intermediate states for FM, Hund's coupling within d orbitals gain energy so that FM states are stable compared to AFM states. Apart from the regular super-exchange contributions which may be valid for fully occupied Cr $t_{2\mathrm{g}}^{3\uparrow}$ states, the presence of the hybridized Te p holes generated by the strong $dp\sigma$-hybridization between Cr d and Te p orbitals plays a crucial role in the FM-coupling mechanism in this class of TMTC materials. The itinerant holes residing in the Te p ligands are coupled to their neighboring Cr spins antiferromagnetically, mediating the FM ordering of Cr local moments. This mechanism shares a common feature with the Zener's mechanism[65] where an effective exchange interaction is generated by the sd-hybridization instead of the pd-hybridization. Therefore, to stabilize the FM ordering of Cr spins, it is essential to have the energy gain by the negative polarization of the p state, which is considered as a relaxation of the non-magnetic elements.

To help the understanding of the electronic structure of TMTC, we present a schematic energy diagram for $CrSiTe_3$ in Fig. 3.4. This diagram may serve as a representative picture for the electronic configuration of 2d TMTC materials.

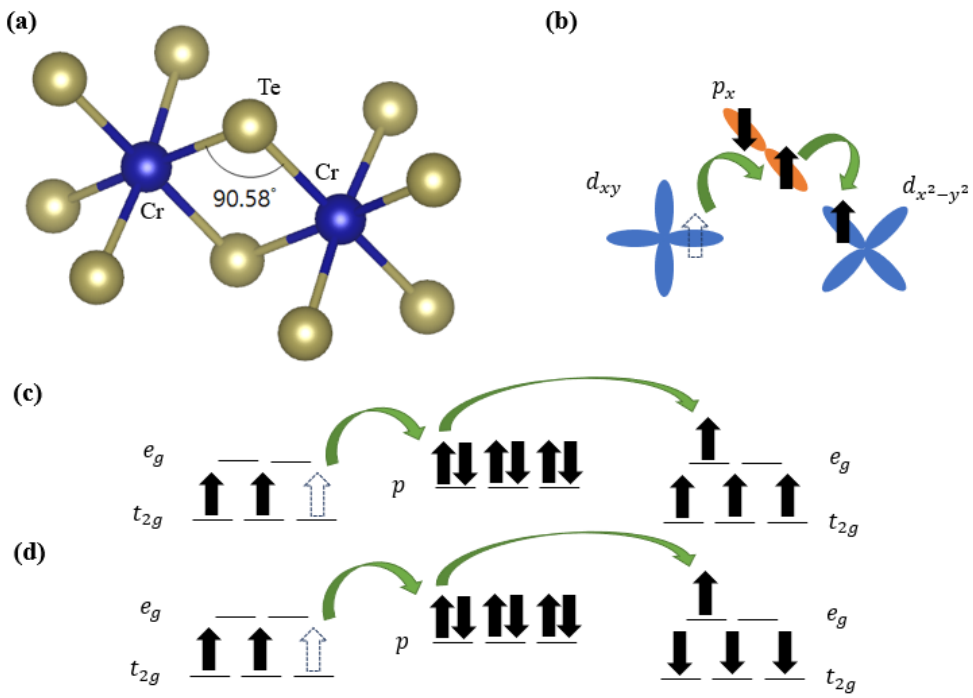

Figure 3.3 (Color online) (a) Near 90^o of Cr-Te-Cr bonding angle, (b) hopping path from Cr occupied t_{2g} orbitals to adjacent Cr empty e_g orbitals via p orbital, intermediate state of virtual hopping process of (c) FM and (d) AFM states.

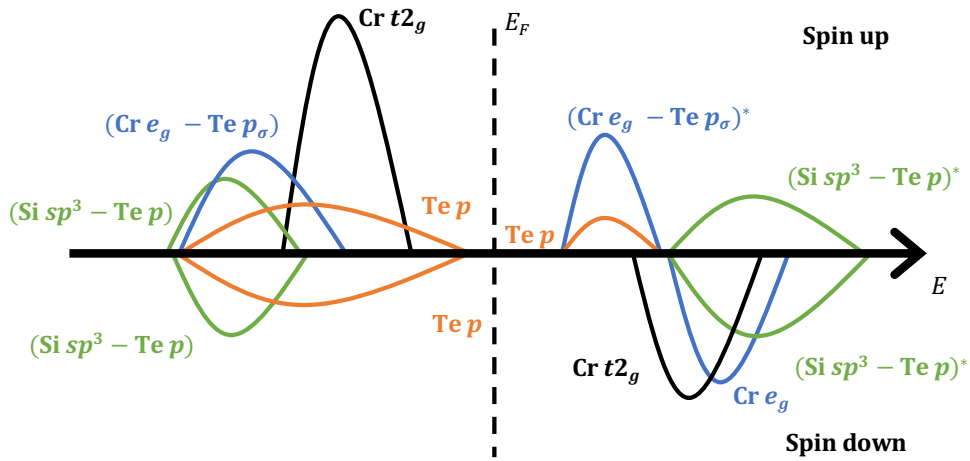

Figure 3.4 (Color online) Schematic energy diagram of the $CrSiTe_3$ electronic structure. The primary features are the bonding and antibonding bands of (Cr e_g-Te $p\sigma$) and (Si sp^3-Te p) hybridized states, whereas the localized Cr t_{2g} bands are split into the spin-up and spin-down channels across the Fermi level (E_F).

As we discussed above, each Cr e_g orbital form a bonding and anti-bonding pair of (Cr e_g - Te p_σ) states, whereas the weak $dp\pi$ hybridization leads to the localized Cr t_{2g} states. One notable feature is that the Si $3s$ level is located at -6.5 eV below E_F, which is not shown in Fig. 3.2. Since the Si atom has the tetrahedral coordination surrounded by another Si atom and 3 Te atoms, the Si sp^3 hybrid orbitals can make a strong bonding and antibonding pair of (Si sp^3 - Te p). Hence, the bandgap in the spin-up channel is formed between the Cr e_g conduction band and the Te p valence band for both $CrSiTe_3$ and $CrGeTe_3$. The principal components near the top of the valence bands consist of the anti-bonding Te p - Te p character, while the conduction bands are from the anti-bonding Cr e_g - Te p orbitals.

3.3.2 On-site U and Magnetic Ground States of $CrBTe_3$ (B = Si, Ge)

From the results of calculations with varying U, we observe an interesting but still critical behavior of bandgap as well as magnetic order depending on the on-site Coulomb interaction for Cr d orbital states. As illustrated in Fig. 3.5(a) and (b), the change of the indirect and direct bandgaps with varying on-site U parameters demonstrates that the bandgaps are sensitive to the choice of the U values for $CrSiTe_3$ and $CrGeTe_3$ monolayer as well as bulk systems. For example, the $U = 0$ calculations show an insulating ground state with finite gaps, while $U = 3$ eV predicts a semi-metallic ground state with negative indirect gaps for both $CrSiTe_3$ and $CrGeTe_3$. This U-dependence can be understood from the electronic structures near E_F.

The increase of U pushes down the localized spin-up Cr t_{2g} level relative to the unoccupied Cr e_g - Te p hybridized state. But, the top of the valence bands, consisting mostly of the Te p component, is not affected by the change of U. The downward shift of the t_{2g} level in turn raises the anti-bonding Te p bands. Thus, the increases of U contributes to the relative upward shift of the anti-bonding Te p bands, thereby leading to the decrease of the indirect and direct bandgaps. The smaller bandgaps for the bulk systems are attributed to the large bandwidth of the Te p bands, which reflect the overlap of Te p states across the layers.

Thus, the choice of U for the Cr $3d$ orbitals is crucial in the determination of their ground state. Along with the change of bandgaps, the U-parameters also affect the magnetic ordering between the layers. While the single-layer $CrSiTe_3$ and $CrGeTe_3$ favor the FM ground state, the interlayer magnetic

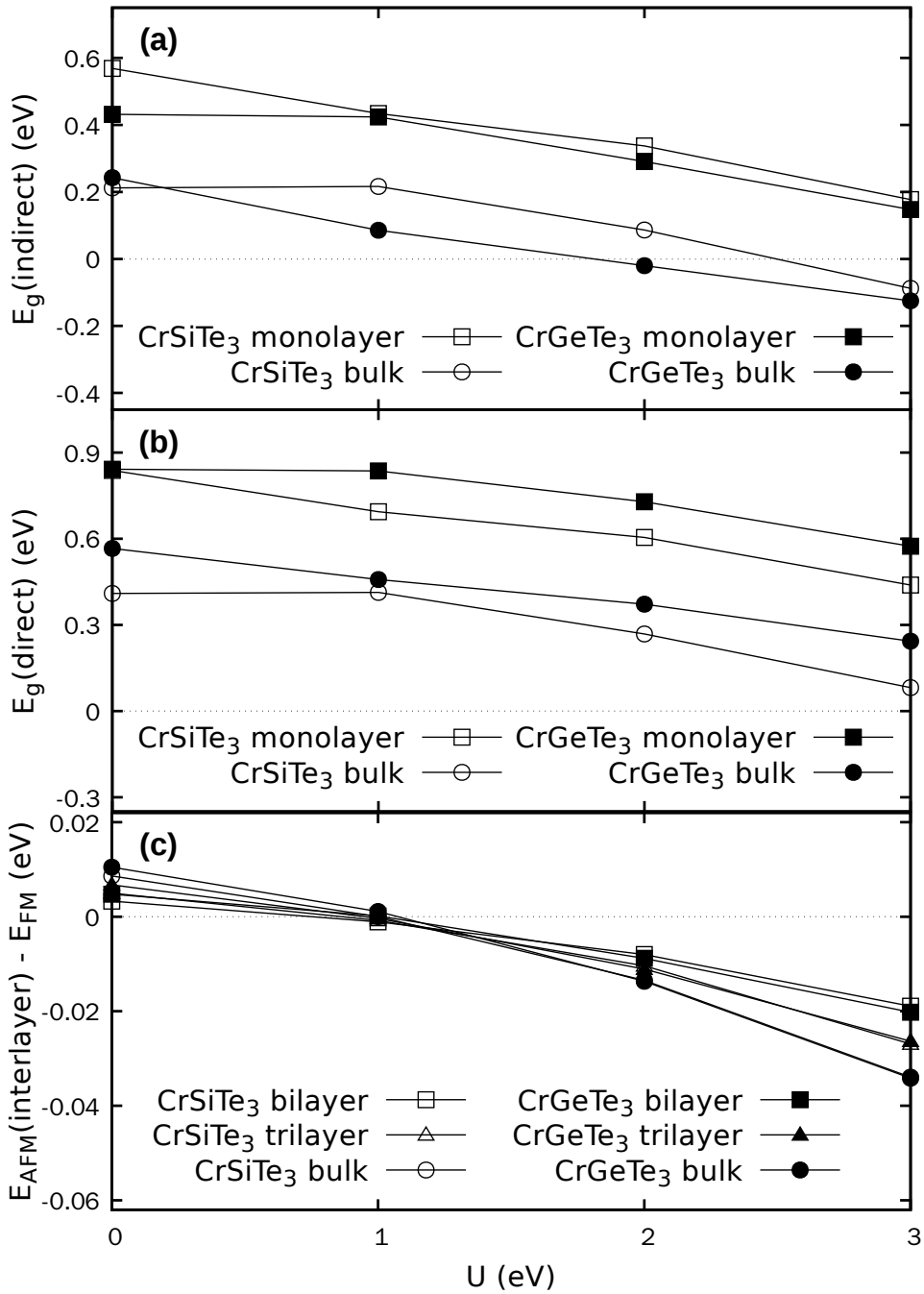

Figure 3.5 (a) Indirect and (b) direct bandgaps for the monolayer and bulk $CrSiTe_3$ and $CrGeTe_3$ systems and (c) total energy differences between the A-type (i.e., interlayer-antiferro) antiferromagnetic (AFM) and the ferromagnetic (FM) for bilayer, trilayer and bulk $CrSiTe_3$ and $CrGeTe_3$ depending on the on-site Coulomb interaction parameter U.

couplings are prone to the on-site Coulomb interaction at the Cr site. Fig. 3.5(c) shows that the FM ground state is stable only for $U < 1.0$ eV and the antiferromagnetic (AFM) order takes over for $U > 1.0$ eV. In the case of $3d$ transition-metal oxides, $U = 3.5$ eV was reported for Cr_2O_3, for instance, from GGA+U calculations in comparison with experiments[66]. However, if $U = 3.5$ eV were adopted for TMTC, both $CrSiTe_3$ and $CrGeTe_3$ would be a semi-metal with a negative bandgap, which contradicts to the semiconducting behavior observed in experiment[32, 58, 67–69]. Therefore, in the range of $U < 1.5$ eV, we conclude that both bulk $CrSiTe_3$ and $CrGeTe_3$ may have the FM or A-type AFM ground state, where the interlayer AFM coupling can be small compared to the intralayer FM couplings. In particular, it is noted in Fig. 3.5(c) that the interlayer coupling becomes almost zero near U 1.0 eV. Further, a recent spectroscopic measurement study also support the reduced value of U[70].

Choice of Hubbard U parameters also affect to magnetic ground state in $CrSiTe_3$ and $CrGeTe_3$ monolayer. Fig. 3.6 shows magnetic ground state of using U as 1.5 eV and 4.0 eV for $CrSiTe_3$ and $CrGeTe_3$ monolayer. Under condition of $U = 1.5$ eV, the magnetic ground state is FM for both $CrSiTe_3$ and $CrGeTe_3$ monolayer. However, magnetic ground state changes to AFM(zigzag configuration) in $CrSiTe_3$ monolayer for $U = 4.0$ eV, whereas FM ground state maintains in $CrGeTe_3$ monolayer. It implies that Hubbard U parameters play crucial role of determining magnetic ground state in $CrSiTe_3$ monolayer. In addition, one may conclude FM ground state in monolayer of $CrSiTe_3$ and $CrGeTe_3$ by choosing U as 1.5 eV which makes good agreement in experimental results[70].

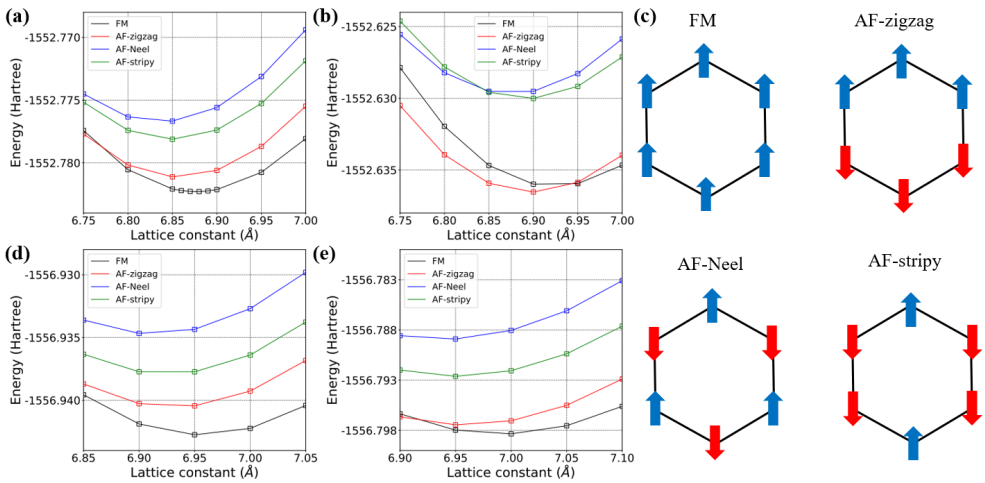

Figure 3.6 (Color online) Total energy as a function of in-plane lattice constant a of $CrSiTe_3$ monolayer using Hubbard U parameters as (a) U = 1.5 eV, (b) U = 4.0 eV, respectively. (c) Schematic of spin ordering of magnetic configurations used in total energy calculations (blue and red arrow indicate up- and down-spin, respectively). Total energy as a function of in-plane lattice constant a of $CrGeTe_3$ monolayer using Hubbard U parameters as (d) U = 1.5 eV, (e) U = 4.0 eV, respectively.

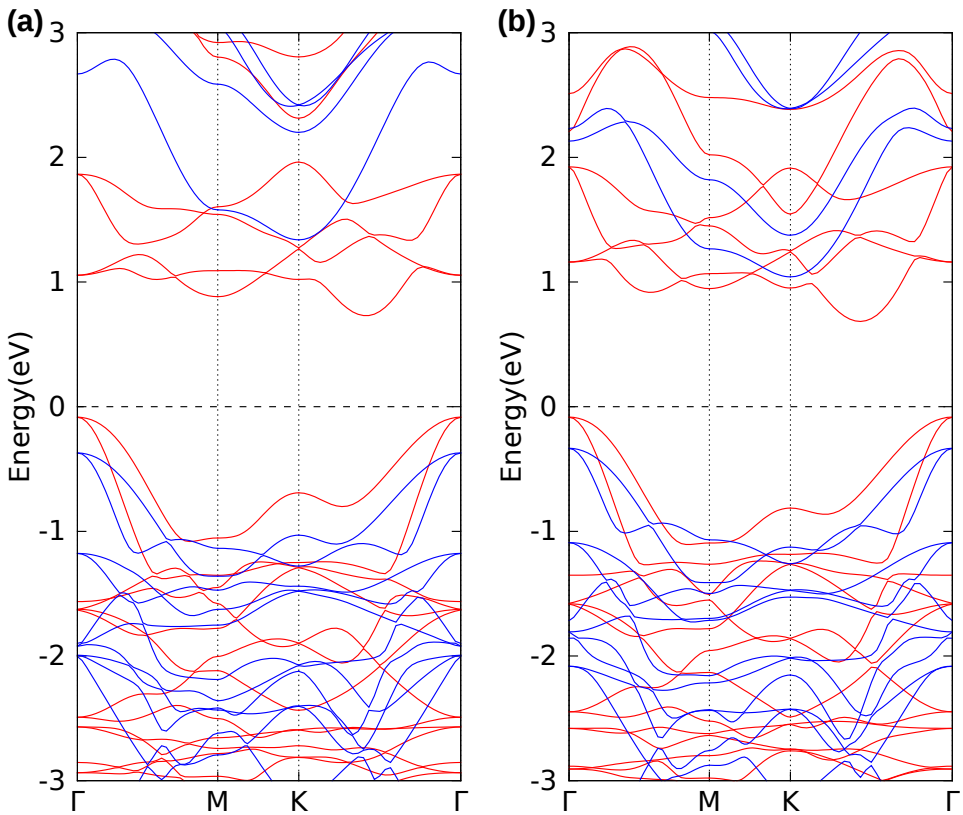

Figure 3.7 (Color online) Band structure calculated by using HSE06 hybrid functional for (a) $CrSiTe_3$ and (b) $CrGeTe_3$ monolayer. Red and blue lines indicate up-spin and down-spin components, respectively.

As a reference, we obtained the bandgaps from HSE06 hybrid-functional calculations depicted in Fig. 3.7. The HSE06 indirect and direct bandgaps for the single-layer $CrSiTe_3$ are 0.85 eV and 1.18 eV, which are significantly larger than the $U = 0$ eV results of 0.57 eV and 0.84 eV, respectively, as illustrated in Fig. 3.5. Similarly, the HSE06 indirect (0.77 eV) and direct (1.24 eV) bandgaps for the single-layer $CrGeTe_3$ are larger than the $U = 0$ eV results of 0.43 eV and 0.84 eV, respectively. Despite the larger bandgaps, the overall features of the electronic structures of the HSE06 hybrid-functional calculations are consistent with the small U results. Since the HSE06 bandgaps for transition metal oxides and chalcogenides have a complication treating localized $3d$ electrons[71, 72], however, it may require further investigations to understand the origin of such reduced U for TMTC.

3.4 Conclusion

To understand the electronic and magnetic properties of 2d TMTC materials especially of $CrSiTe_3$ and $CrGeTe_3$, we performed DFT calculations within the GGA+U method. The single-layer $CrSiTe_3$ and $CrGeTe_3$ are found to be a FM insulator with a small but finite bandgap for $U < 1.5$ eV. The total magnetic moment per formula unit is 3 μ_B. However, the local magnetic moment of each Cr atom is determined to be 3.87 μ_B for $U = 1.5$ eV, where the extra contribution of 0.87 μ_B comes from the $dp\sigma$ bonding states of Cr e_g - Te p. It is remarkable that the -0.3 μ_B spin polarization resides at each Te atom as a result of the strong Cr - Te $dp\sigma$ hybridization. This negative polarization of Te p relative to Cr evidences that the strong $dp\sigma$-hybridization of Cr e_g - Te p is crucial for the stabilization of FM ordering of Cr ions. In addition to

the presence of Te p holes due to the strong Cr - Te dp-hybridization, the role of the on-site Coulomb interaction U for Cr d electrons seems to be different from the case of $3d$ transition metal oxides. The bandgaps for both $CrSiTe_3$ and $CrGeTe_3$ decrease significantly as U increases. In fact, the bandgaps are formed between the Cr e_g conduction band and the Te p valence band for both $CrSiTe_3$ and $CrGeTe_3$. The dominant Te p anti-bonding bands in the valence bands just below the Fermi level is related to the decrease of the bandgap for the increase of U. Besides the U-dependent bandgaps, the magnetic ground state is also sensitive to U. As illustrated in Fig. 3.5, the interlayer magnetic coupling in both bulk and multilayers of $CrSiTe_3$ and $CrGeTe_3$ can be FM for $U < 1.0$ eV or A-type AFM for $U > 1.0$ eV. Further, $U \approx 1.0$ eV, the energy difference between FM and A-type AFM is negligile, and the magnetic response becomes critical. In addition, $CrSiTe_3$ monolayer shows U-dependent in-plane magnetic ground state. Thus, the magnetic ordering of the TMTC materials may be sensitive to external fields or strains. We hope that our findings serve for the future experimental measurements, which will help our understanding of electronic and magnetic properties of TMTC materials.

Chapter 4

Field-controlled quantum anomalous Hall effect in electron doped $CrSiTe_3$ monolayer

In this chapter, we consider topological properties of $CrSiTe_3$ ferromagnetic monolayer in the presence of electron doping. We investigate crossing points within Cr e_g conduction bands manifold and calculate Berry curvatures after band gap opening induced by spin-orbit coupling effect. Furthermore, we check that the anomalous Hall conductivity and magnetic anisotropy energy depends on direction of magnetic ordering. We draw Berry curvatures in momentum space and electronic band structure by changing spin angle to analyze topological properties as well as localized moment picture in electron doped $CrSiTe_3$ ferromagnetic monolayer.

4.1 Introduction

The nontrivial topology of electronic band structure can give rise to many novel phenomena. In 2d system, the representative example is Quantum Hall

effect (QHE) which shows quantized Hall conductivity for two 2d electrons under external magnetic field. Another example is Haldane model suggested by Haldane in 1988[14]. A Chern insulator is such a topological state of matter exhibiting a nonzero quantized Hall conductivity without an external magnetic field. It shows QAHE characterized by $\mathbf{Z}$ topological invariant, i.e. Chern numbers, unlike time-reversal-symmetric conventional topological insulators classified by $\mathbf{Z}_2$-invariants such as Bi_2Se_3, Bi_2Te_3, Sb_2Te_3[29] or HgTe[30]. In recent study, transition metal tri-chalcogenides are suggested as candidate of Chern insulator with high Chern numbers[24]. It shows multiple Dirac cones in e_g bands manifold which leads to high Chern numbers by considering SOC effect.

In this work, we report that $CrSiTe_3$ monolayer also shows the Chern insulating phases with high Chern numbers which can be realized by electron-doping. We find crossing points within the Cr e_g conduction band manifolds, where the crossings are removed as spin-orbit-coupling (SOC) is introduced and leading to topologically nontrivial bands with Chern number up to 8. We also find quantized anomalous Hall conductivity (AHC) at one- and two-electron-doping per unit cell, which can be further varied as spin orientation angle changes. Additionally, it is found that the magnetic anisotropy energy is suppressed as electron doping is introduced, consistently with a recent findings[73, 74], which makes tuning of AHC via external magnetic field feasible. Our result reveals that single-layers of magnetic $CrSiTe_3$ is promising platforms to realize Chern insulating materials with high Chern numbers and show field controlled quantum anomalous Hall conductivity under electron doping.

4.2 Computational Details

4.2.1 Density Functional Theory Calculations

To obtain band structures and pDOS, we perform *ab initio* electronic structure calculation based on density-functional theory (DFT) using OPENMX[59, 60] code, which employs linear-combination-of-pseudo-atomic-orbital basis with norm-conserving pseudopotentials. We choose generalized gradient approximation (GGA) exchange-correlation functional in the parameterization of Perdew, Burke and Enzerhof (PBE)[38] with Hubbard U parameters chosen to be 1.5 eV for Cr d orbital. SOC effects are included in the calculations via fully-relativistic pseudopotentials implemented in OPENMX[59, 60]. Pseudo-atomic orbitals are set to be $s^3p^2d^2$ for Cr, $s^2p^2d^1$ for Si, $s^3p^3d^2$ for Te, respectively. To simulate two-dimensionality, we insert 20 Å of vacuum in the unit cell. $10 \times 10 \times 1$ of k-space mesh is adopted for the momentum space integration. Energy cutoff for choosing real-space grid is set to be 700 Ry ($96 \times 96 \times 360$ real space grid). 10^{-6} Hartree/Bohr of force criterion is chosen for the optimization of internal coordinates while keeping C_3 rotation, inversion and mirror symmetries. SOC effects are excluded in the process of structural relaxation. We fix Bravais lattice as hexagonal and determine lattice constant by performing total energy minimization calculation as a function of unit cell size.

4.2.2 Analysis of Topological Characteristics

Berry curvature is given by

$$B_n(\mathbf{k}) = i \sum_{n' \neq n} \frac{\langle n|\frac{\partial H}{\partial k_x}|n'\rangle\langle n'|\frac{\partial H}{\partial k_y}|n\rangle - (k_x \leftrightarrow k_y)}{(E_n - E_{n'})^2} \tag{4.1}$$

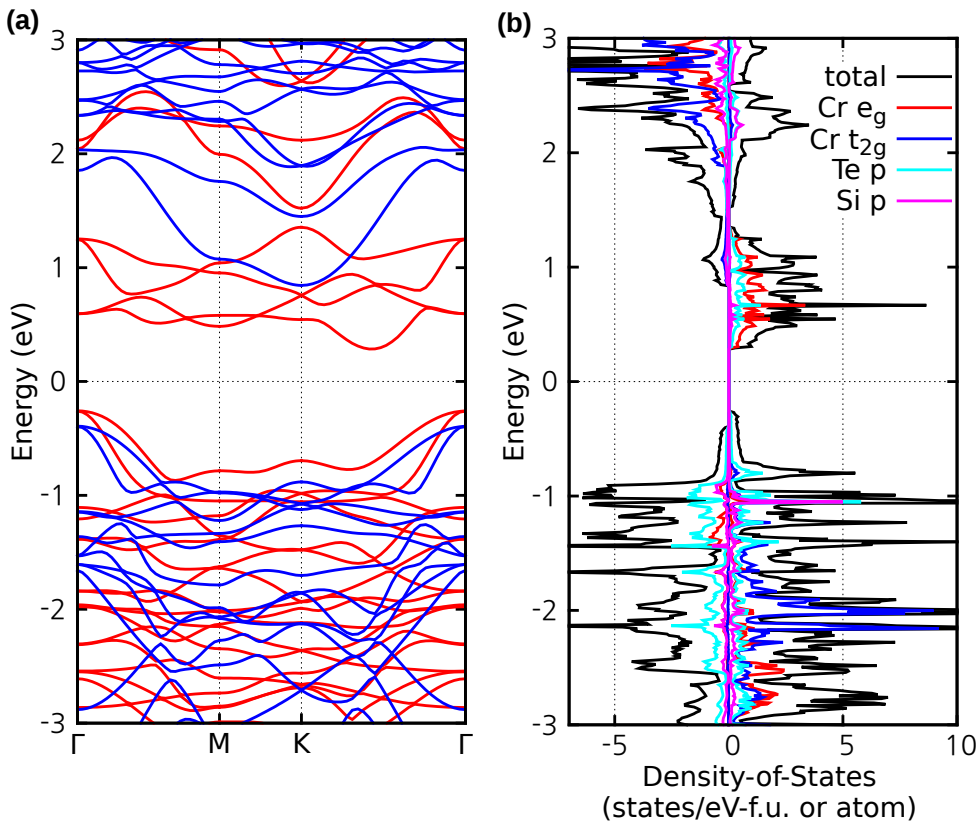

Figure 4.1 (Color online) Band structure and pDOS plot of single layer $CrSiTe_3$ with ferromagnetic state: band structure with majority spin (red line) and minority spin channel (blue line) in (a), respectively. Total density of states (black line), projected density of states of Cr e_g orbital (red line) and t_{2g} orbital (blue line), Si p orbital (purple line) and Te p orbital (sky blue line) are indicated in (b). In pDOS plot, plus and minus sign correspond to majority and minority spin components, respectively. Fermi level is set to be zero for both panels.

where integrating Berry curvature in BZ gives Chern number

$$C_n = \frac{1}{2\pi}\iint_{BZ} B_n(\mathbf{k})dk_x dk_y \tag{4.2}$$

E_n is Kohn-Sham eigenenergy of band index n at certain $\mathbf{k}$=(k_x,k_y) point and H is Hamiltonian of system. Anomalous Hall conductivity is calculated by integrating Berry curvatures over BZ up to arbitrary energy level which is given by

$$\sigma_H(E) = \frac{e^2}{h}\iint_{BZ} B_n(\mathbf{k}) f_{FD}(E,\mathbf{k})dk_x dk_y \tag{4.3}$$

where e is electron charge, h is Planck constant and $f_{FD}(E,\mathbf{k})$ is Fermi-Dirac distribution function, respectively. To compute Berry curvatures, anomalous Hall conductivity, Chern numbers, and chiral edge states, maximally localized Wannier function (MLWF) method as implemented in OPENMX is employed[75, 76]. d_{z^2} and $d_{x^2-y^2}$ orbitals at Cr sites are chosen as initial projectors. 10 $\times$ 10 $\times$ 1 k-space grid is chosen for the construction of MLWFs. From the MLWF tight-binding Hamiltonian obtained, WANNIER TOOLS code is used to compute Berry curvature, Chern numbers and edge states[77]. Specifically, we employ Fukui-Hatsugai formalism[78] to compute Berry curvature, and edge state calculations are done employing iterative Green's functions method in the semi-infinite geometry.

4.3 Results and Discussion

4.3.1 Electronic and Magnetic Properties of Stoichimetric $CrSiTe_3$

$CrSiTe_3$ is one of MAX_3-type TMTC compounds. It has a $R\bar{3}$-type stacking of neighboring $CrSiTe_3$ monolayers, where neighboring layers are coupled by vdW interaction. Crystal structure of a $CrSiTe_3$ monolayer is depicted in Fig. 3.1, showing edge-sharing honeycomb network of $CrTe_6$ octahedra and Si-dimers located at the centers of Cr-hexagons. In undoped $CrSiTe_3$, Cr cations are in the d^3 (Cr^{3+}) high-spin configuration ($S = 3/2$) with fully occupied t_{2g} orbitals. In addition, strong $dp\sigma$ hybridization between Cr d- and Te p-orbitals gives rise to additional magnetic moment contributions, so that the magnitude of Cr spin moment is 3.87 μ_B[50]. The ferromagnetic ground state can be attributed to the Goodenough-Kanamori-Anderson (GKA) superexchange mechanism[63, 64]. Our results are in agreement with previous reports[8, 31, 58] where choice of Hubbard U parameters is crucial for determining magnetic ground state of $CrSiTe_3$[50] and reproducing photoemission spectrum data in $CrGeTe_3$[70].

When electron doping is introduced, orbital occupation of $CrSiTe_3$ changes so that magnitude of magnetic moment of Cr d orbitals as well as lattice constant is also affected. With two electron doping per unit cell, Cr e_g orbital of spin majority channel become half-filled so that the high-spin Cr^{2+} ($S = 2$) configuration is obtained (additional moment of 0.51 μ_B further induced due to $dp\sigma$-hybridization). With this electron doping, the in-plane lattice parameter a expands to be 7.26 Å, 5.7% larger than that of undoped case[6, 31, 50].

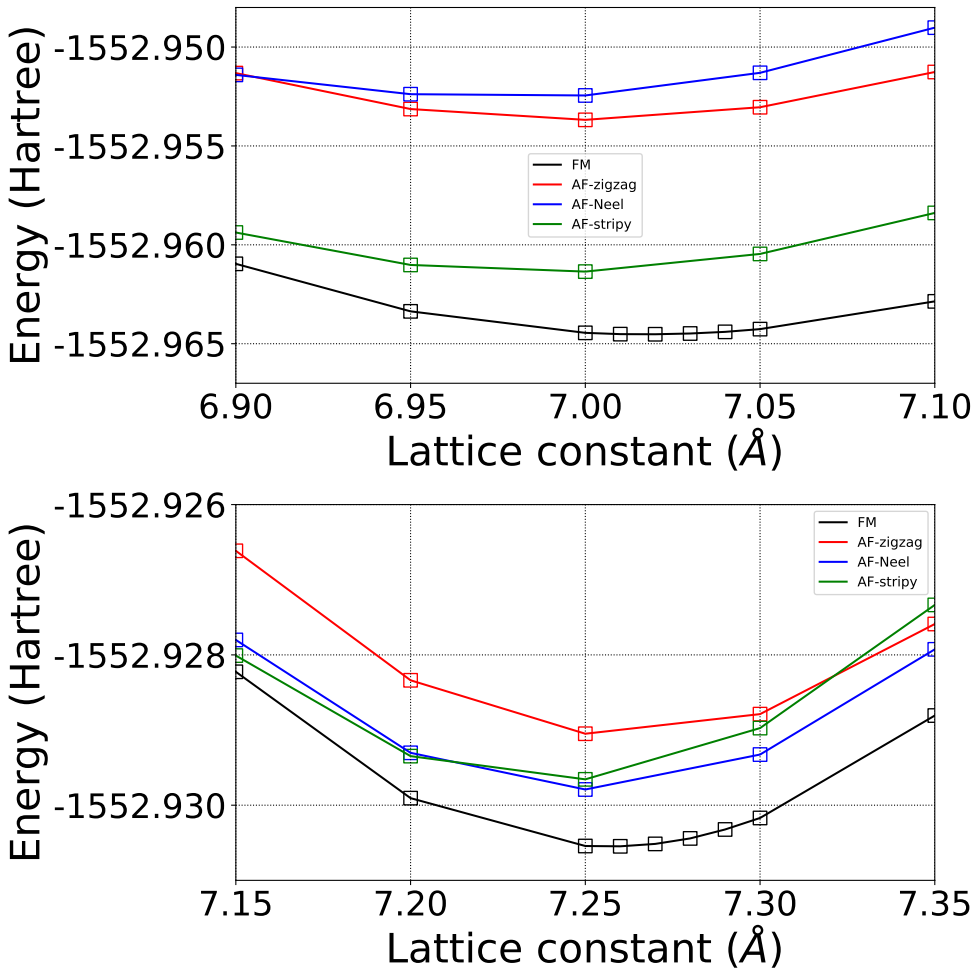

Figure 4.2 (Color online) Total energy as a function of in-plane lattice constant of $CrSiTe_3$ monolayer under one electron doping in unit cell (a) and two electron doping in unit cell (b), respectively.

We check that ferromagnetic ground state with insulating properties and also topological phases remain unchanged within the Hubbard U parameters and lattice constant range of 0.5 eV $\leq U \leq$ 1.5 eV and 6.88 Å $\leq a \leq$ 7.26 Å, respectively. Fig. 4.2 shows total energy calculation results of FM and various AFM configurations under electron doping which demonstrates FM is magnetic ground state. Therefore, hereafter we choose the lattice constant and Hubbard U parameters to be 7.0 Å and 1.5 eV, respectively, as a representative case.

4.3.2 Band Crossings in $CrSiTe_3$ e_g Conduction Bands

To study magnetic and topological properties of electron-doped monolayer $CrSiTe_3$ in the FM state, we first focus on the electronic structure of undoped $CrSiTe_3$. Fig. 4.1 describes band structures and pDOS of ferromagnetic single layer $CrSiTe_3$. Spin majority and minority components shows exchange splitting where spin minority parts have large band gap energy compared to spin majority parts. Right above the Fermi level, four spin majority bands consisting of Cr e_g- and Te p-orbitals exist and are separated from other bands (except Cr t_{2g} bands in the spin minority channel). Interestingly, band crossings are found within the e_g bands, at Γ, K points and on the Γ-M, Γ-K high-symmetry lines as shown in Fig. 4.3. This observation suggests the possibility for the monolayer $CrSiTe_3$ to host nontrivial band topology in the presence of electron doping and gap opening via SOC, as discussed in the following section.

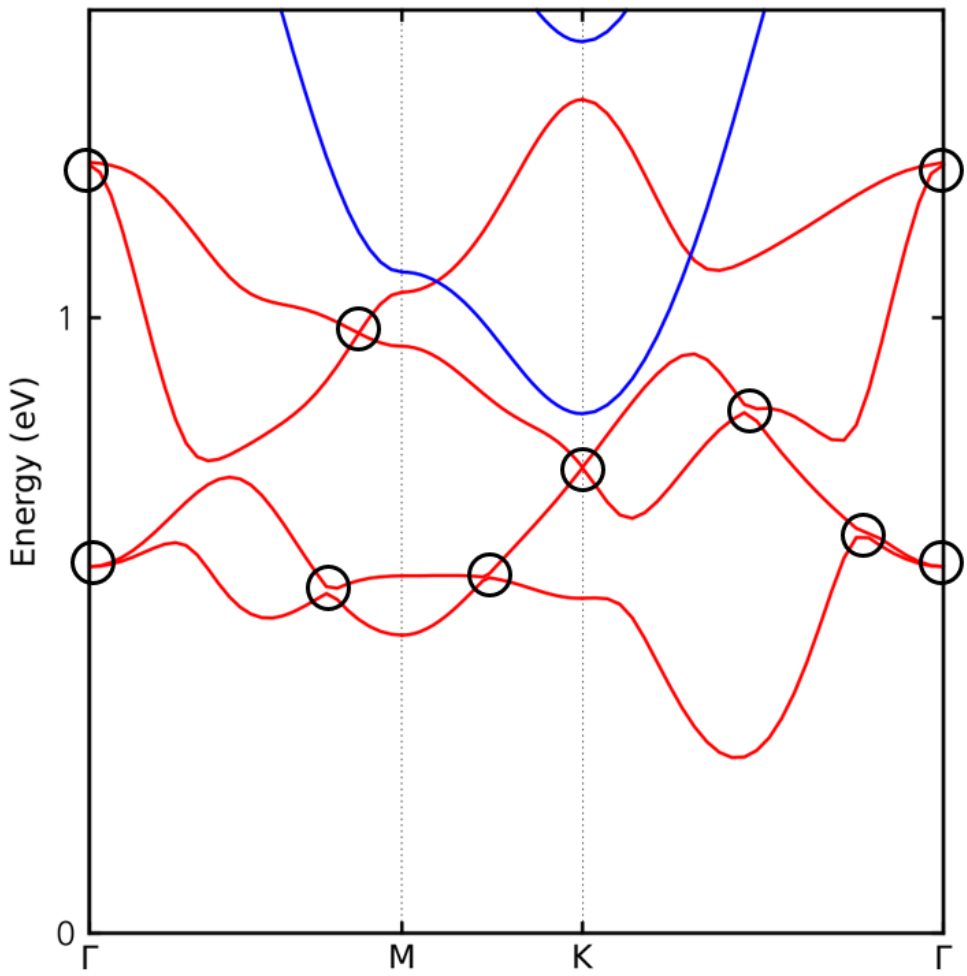

Figure 4.3 (Color online) Cr e_g bands manifold with majority spin component (red lines) in ferromagnetic monolayer of $CrSiTe_3$. Band crossing points are indicated as a black circle. Blue lines are down spin components of band structures.

4.3.3 Berry Curvatures, Chern Numbers and Chiral Edge States

Fig. 4.7 shows magnified Cr e_g band structures with Chern numbers assigned to each bands, plots of Berry curvature in the momentum space, and edge spectra in the presence of integer electron doping, SOC, and out-of-plane ferromagnetic spin orientation. We consider the cases of one and two electron doping per unit cell, where both systems are insulating as shown in Fig. 4.7(a) and (d). For each band, we find unusually high Chern numbers of up to 8, with about 10 meV order of SOC-induced band gap mostly originating from Te p orbital contributions. Fig. 4.7(b) and (e) present Berry curvature of occupied Cr e_g band in the presence of one and two electron doping per unit cell, respectively. In the presence of one electron doping per unit cell (Fig. 4.7(b)), peaks of positive Berry curvature for the lowest Cr e_g band appear around Γ point and on the Γ - M lines, while negative peaks appear close to K and K' points, yielding the Chern number of 2 for the lowest e_g band. In the case of half-filled e_g (Fig. 4.7(e)), two peaks of negative Berry curvature are located at K and K' points, in addition six negative peaks located in between six Γ - K lines, resulting in total Chern number of -4. Fig. 4.7(c) and (f) show edge spectra from the one and two electron doping (per unit cell) results, respectively. Consistently with the Chern number calculation results, one can find two and four chiral edge states near Fermi level in Fig. 4.7(c) and (f), respectively. In Fig. 4.1(a) which shows band structure without SOC effect, lowest and second lowest Cr e_g band are touching at Γ point with quadratic dispersion whereas along Γ - M and M - K line with linear dispersion. Quadratic band touching at Γ point can carry ± 2 topological monopole charge[79] which gives lowest

band Chern number while components of along Γ - M and M - K line with linear dispersion cancel to each other. Between second and third Cr e_{g} bands, crossing at K point and midpoint of Γ - K line has linear dispersion always having its own pair in BZ. Therefore, each linear band crossing impose ±0.5 topological charge[79]. Finally, total 8 peaks of Berry curvature exist in BZ with same sign which can explain total Chern number of half-filled Cr e_{g} band case. Emergence of multiple band crossings in Cr e_{g} bands as shown in Fig. 4.1(a) give rise to nontrivial topology with high Chern numbers. Explanation of microscopic origin of multiple Dirac cones in previous theoretical work[24] can also be applied in our case, where condition of parameters such as hopping integrals is almost equivalent. Calculation results of $CrSiTe_3$ are listed in table 4.1. In addition, descriptions for band gap closing at midpoint of Γ - K line are discussed in following paragraph. To understand features, we start with a simple tight-binding approach as a toy model. If we consider s band like orbital with NN hopping in a honeycomb lattice such as graphene case, the Dirac cone appears at the K point. When 2^{nd} and 3^{rd} NN hopping are taken into account, the Hamiltonian is given by following expressions which becomes more complicated than graphene case,

$$H(\mathbf{k}) = \begin{pmatrix} g(\mathbf{k}) & f(\mathbf{k}) \\ f^*(\mathbf{k}) & g(\mathbf{k}) \end{pmatrix}. \tag{4.4}$$

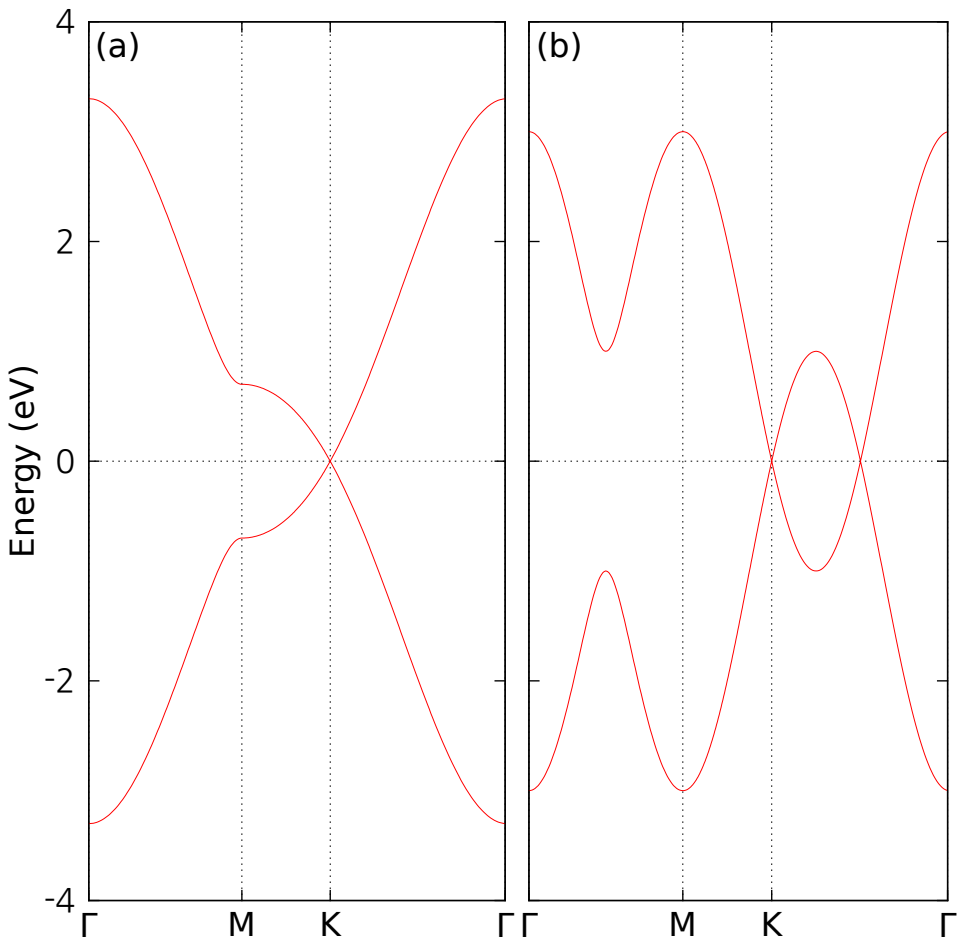

Figure 4.4 (Color online) Band structure plot of simple s orbital like two band tight-binding model regarding 1^{st}, 2^{nd} and 3^{rd} NN hopping under condition of (a) dominant 1^{st} NN hoping ($t_1 >> t_3$) and (b) dominant 3^{rd} NN hoping ($t_1 << t_3$). The 2^{nd} NN hopping term is set to be zero because it only affects energy shift of band diagram where overall features of band dispersion are remain unchanged.

Component of above Hamiltonian $f(\mathbf{k})$ and $g(\mathbf{k})$ is written by

$$\begin{aligned} f(\mathbf{k}) &= t_1[e^{ik_ya/\sqrt{3}} + 2e^{-ik_ya/2\sqrt{3}}cos(k_xa/2)] \\ &\quad + t_3e^{ik_ya/\sqrt{3}}(2cos(k_xa) + e^{-\sqrt{3}ik_ya}) \\ g(\mathbf{k}) &= t_2[2cos(k_xa) + 4cos(k_xa/2)cos(\sqrt{3}k_ya/2)], \end{aligned} \tag{4.5}$$

where $\mathbf{k} = (k_x, k_y)$, a is lattice constant and t_i is i^{th} NN hopping parameters. Diagonalizing the Hamiltonian expressed in Eq. (4.4), one can obtain equation of eigenenergy function as follows.

$$\begin{aligned} E(\mathbf{k}) = t_2(2cos(k_xa) + 4cos(k_xa/2)cos(\sqrt{3}k_ya/2)) \pm \big[(t_1 + 2t_3cos(k_xa)^2 \\ + (t_1 + 2t_3cos(k_xa))(4t_1cos(k_xa/2)cos(\sqrt{3}k_ya/2) + 2t_3cos(\sqrt{3}k_ya)) \\ + (2t_1cos(k_xa/2))^2 + {t_3}^2 + 4t_1t_3cos(k_xa/2)cos(\sqrt{3}k_ya/2)\big]^{1/2} \end{aligned} \tag{4.6}$$

In this case, additional crossing point appears near the midpoint of Γ - K line under the condition of large 3^{rd} NN hopping parameter compared to 1^{st} and 2^{nd} NN hopping terms. This features are depicted in fig. 4.4.

$(i,\ j)$	${t^{(1)}}_{ij}$	${t^{(2)}}_{ij}$	${t^{(3)}}_{ij}$	${t^{(4)}}_{ij}$	${t^{(5)}}_{ij}$
$d_{x^2-y^2}$, $d_{x^2-y^2}$	-27.97	6.7	175.08	-2.42	36.94
$d_{x^2-y^2}$, d_{z^2}	2.55	14.46	10.21	1.76	0.64
d_{z^2}, $d_{x^2-y^2}$	1.51	13.7	3.65	1.77	1.09
d_{z^2}, d_{z^2}	-8.82	-18.03	-20.36	12.49	-14.85

Table 4.1 Hopping parameters based on converged MLWF basis. ${t^{(n)}}_{ij} = \langle\, \mathrm{i}, 0 \mid \hat{H} \mid \mathrm{j}, \mathbf{r_n} \,\rangle$, where i, j index indicates pair of MLWFs and $\mathbf{r_n}$ is cell displacement vector which corresponds to n^{th} NN site. Unit of hopping parameters is meV.

Table. 4.1 shows overlap matrix from our MLWF calculation results. One can find large 3^{rd} NN term compare to other terms which satisfies condition

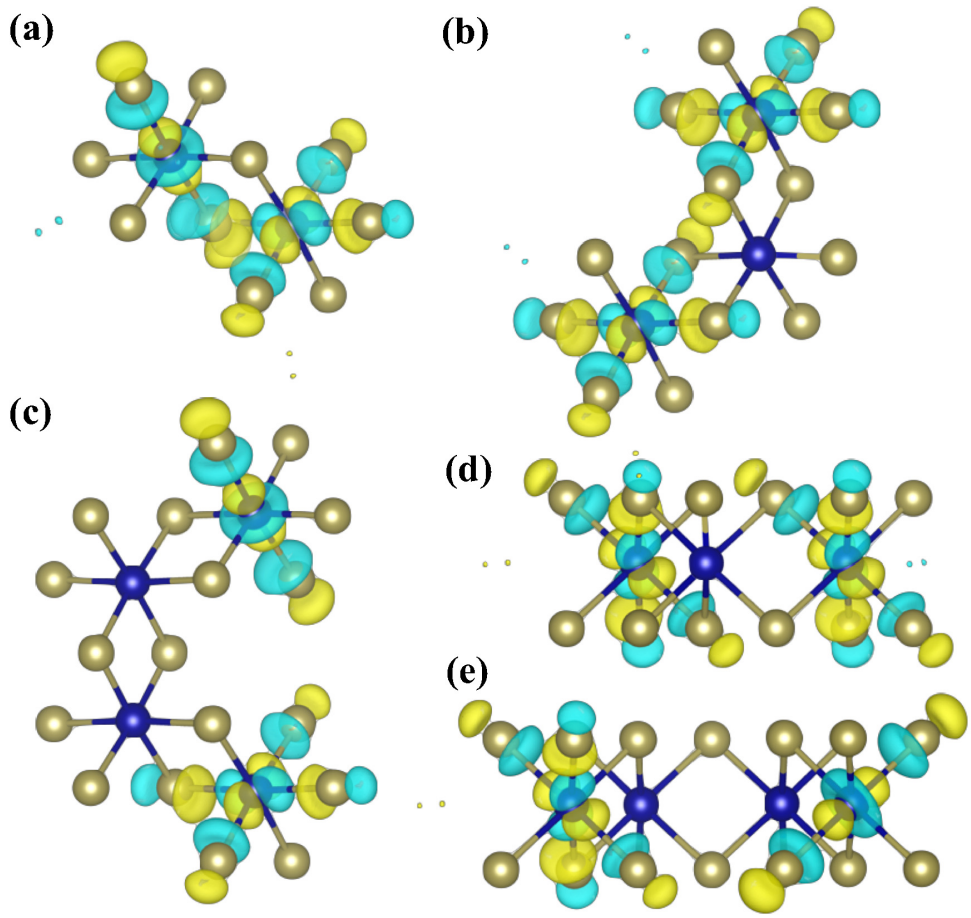

Figure 4.5 (Color online) Converged MLWF plot of e_g band manifold hybridized with Te p states together with neighboring $CrTe_6$ octahedron: (a) top view of Nearest neighbor(NN), (b) 2^{nd} NN, (c) 3^{rd} NN and (d) side view of 2^{nd} NN, (e) 3^{rd} NN, respectively.

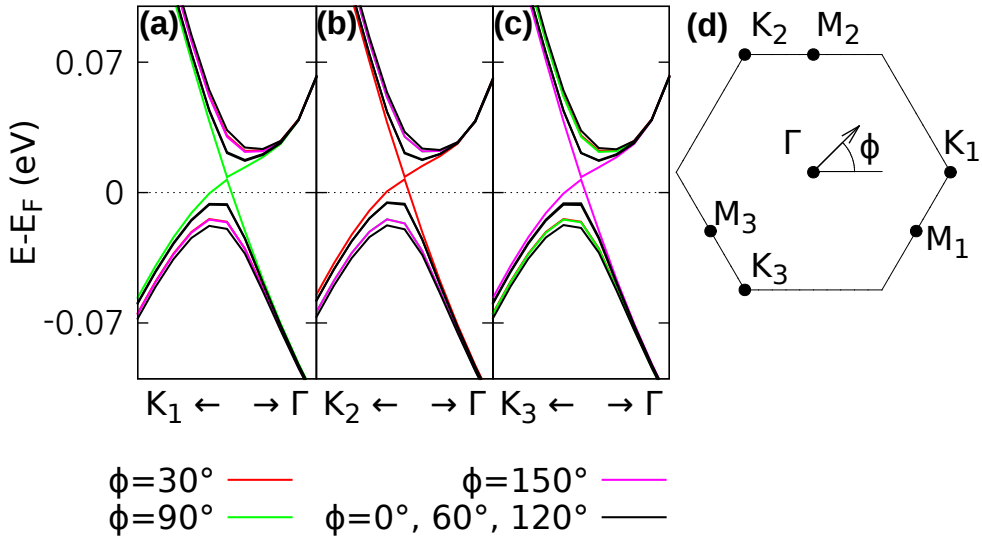

Figure 4.6 (Color online) Band structure with easy plane spin configuration under two electron doping for various in-plane spin angle which is especially expanded near middle of (a) Γ - K_1, (b) Γ - K_2 and (c) Γ - K_3 line, respectively. (d) First BZ with high symmetry points and in-plane spin angle ϕ.

of above simple model approach. It can be confirmed qualitatively in Fig. 4.5 which shows converged MLWF graphically. Hopping between NN sites is small due to orthogonality of mediating Te p orbitals. For 2^{nd} and 3^{rd} NN hopping, mediating two Te p orbitals are located in different layer for 2^{nd} NN case while in same layer for 3^{rd} NN case which induces much large 3^{rd} NN hopping parameters compared to 1^{st} and 2^{nd} ones.

In many cases, band degeneracy is related to the symmetry of system. If spin lies in-plane, its direction has chance to become vertical to one of three mirror planes of $CrSiTe_3$ which contain Γ - K line and perpendicular to its layer. When spin orientation is perpendicular to mirror plane, mirror symmetry would then be restored which is shown in Fig. 4.6. For case of $\phi = 90°$, 30° and 150°, band gap is closing near midpoint of Γ - K_n (where n=1,2,3) line, respectively while still maintaining at other points including K_n points. In

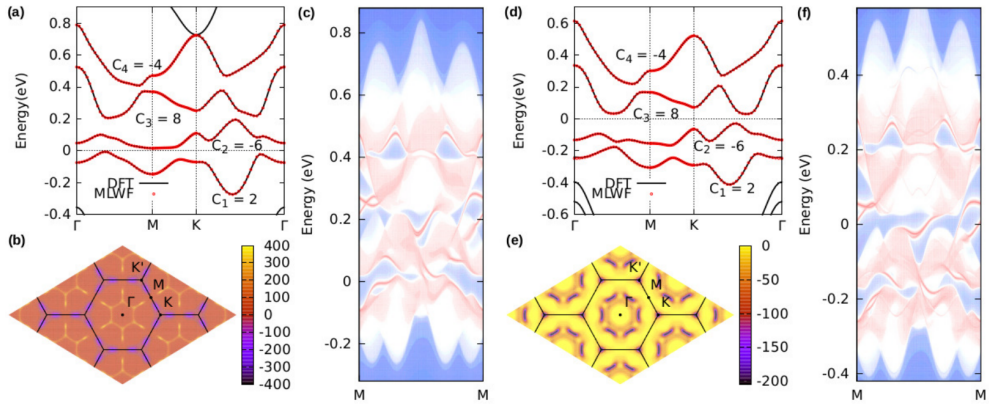

Figure 4.7 (Color online) (a) Cr e_g band manifold using DFT (black line) and Wannier function interpolation (red circle) band structure under one electron doping per unit cell. Chern numbers for each bands are also remarked. (b) Berry curvature plot for occupied Cr e_g band contribution with high symmetry line. Unit of Berry curvature is $1/\text{Å}^2$. (c) Chiral edge states plot along armchair direction under one electron doping per unit cell. Red lines indicate edge states components. Pink regions are bulk states while blue area corresponds to vacuum. (d) Cr e_g band manifold using DFT (black line) and Wannier function interpolation (red circle) band structure under two electron doping per unit cell. Details of figure are equal to figure (a). (e) Berry curvature plot for occupied two Cr e_g band contribution with high symmetry line. (f) Chiral edge states plot under two electron doping per unit cell. Details of figure are equal to figure (c). All figures are drawn under introducing SOC effect with spin aligned to out-of-plane direction.

Fig. 4.6(d), one can confirm each spin angle ($\phi = 30°$, $90°$, $150°$) corresponds to perpendicular to mirror plane (Γ - K_2, Γ - K_1, Γ - K_3), respectively. We may conclude additional crossing points at Γ - K line originated from mirror symmetry of the system, while crossing at K point is from sublattice symmetry which is equivalent with graphene case.

4.3.4 AHC under Electron Doping

We further examine AHC of Cr e_g bands manifold, total density of states of $CrSiTe_3$ and anisotropy energies illustrated in Fig. 4.8. Total AHC shows

quantized plateau at integer number of electron doping, consistent again with the Chern number calculation results in Fig. 4.7(a) and (d). In addition, total density of states vanishes at one and two electron doping as depicted in Fig. 4.8(b). Therefore, Cr e_g bands are separated to each other together with nonzero Chern numbers so that Chern insulating phases will be realized under one or two electron doping in unit cell.

4.3.5 Magnetic Anisotropy and Its Doping Dependence

So far, our DFT calculations with SOC effect are considering spin aligned to out-of-plane direction. However, this out-of-plane spin configurations can be suppressed or become unstable as the electron doping is introduced, because magnetic anisotropy may depend on e_g occupation. Fig. 4.8(c) shows anisotropy energies as a function of electron doping concentrations, which have oscillating behaviors between easy-plane and easy-axis anisotropies. For example, easy-axis anisotropy occurs at one electron doping, while easy-plane anisotropy is favored at two electron doping per unit cell. It is worth mentioning that magnetic anisotropy may vanish as doping is introduced, which may enable tuning the direction of FM moments and the resulting electronic structure via external magnetic fields.

Since spins are magnetic dipoles, magnetic long-range dipole-dipole interactions between local moments may change magnetic anisotropy. Because this inter-dipole interactions are not captured within DFT, we employ Ewald's lattice summation technique to compute dipolar energy and estimate its effect on magnetic anisotropy[80–83]. Magnetic dipole energy is defined as following

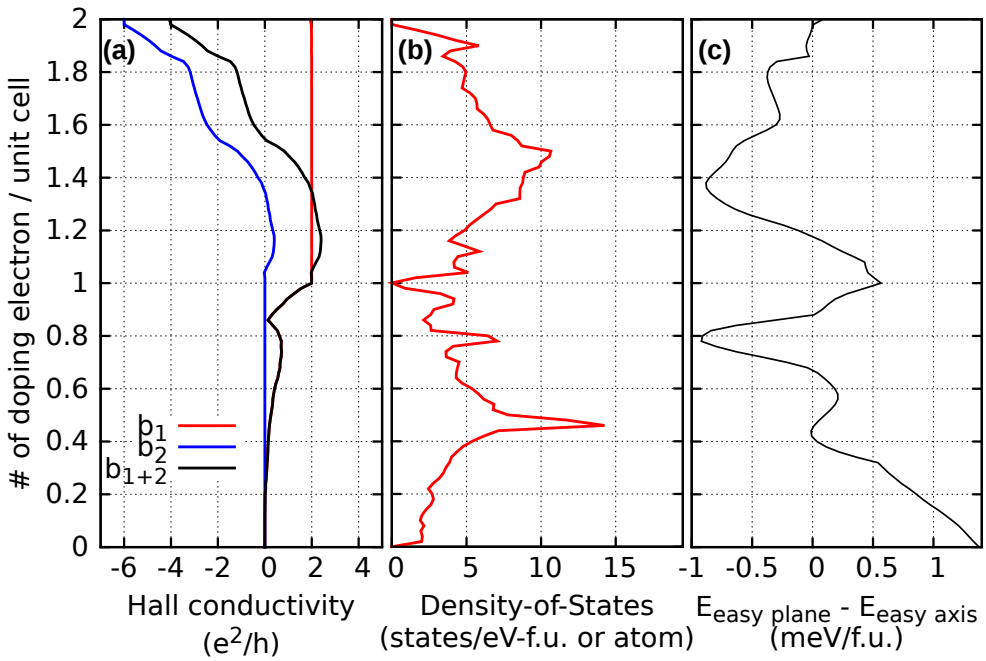

Figure 4.8 (Color online) AHC contributions for each band of Cr $e_{\mathbf{g}}$ band manifolds as a function of electron doping, (a) from the lowest band (red line), second lowest band (blue line) and sum of two bands (black line), respectively. (b) Total density of states of Cr e_{g} bands. Note that results shown in (a) and (b) are obtained in the presence of the out-of-plane spin direction. (c) Energy difference between easy plane and easy axis configurations of single layer $CrSiTe_3$ as a function of electron doping.

equations,

$$E_d = \sum\nolimits_{\mathbf{qq'}} \frac{2m_{\mathbf{q}}m_{\mathbf{q'}}}{c^2} M_{\mathbf{qq'}} \tag{4.7}$$

$$M_{\mathbf{qq'}} = \sum\nolimits_{\mathbf{R}} \frac{1}{|\mathbf{R}+\mathbf{q}+\mathbf{q'}|^3} \left[1 - 3\frac{[(\mathbf{R}+\mathbf{q}+\mathbf{q'})\cdot \widehat{m_{\mathbf{q}}}]^2}{|\mathbf{R}+\mathbf{q}+\mathbf{q'}|^2} \right] \tag{4.8}$$

where $\mathbf{R}$ is lattice vector, $\mathbf{q}$ is atomic position vector of local magnetic moment in unit cell and $m_{\mathbf{q}}$ is local magnetic moment at $\mathbf{q}$, respectively. By using equation 4.7 and 4.8, we calculate magnetic dipolar interaction energy. Magnitude of local magnetic moment in equation 4.7 is estimated by using DFT calculation. Table 4.2 lists magnetic dipolar interactions energies as a function of electron doping concentrations as well as anisotropy energies from DFT calculations. It is shown that dipolar interactions favor the easy-plane configuration over the easy-axis one in FM states (as shown in the negative values of D-MAE in the table). Combining anisotropy energies from DFT (C-MAE) and dipolar interactions (D-MAE), it can be seen that easy-plane spin configurations are more favored except for undoped and one electron doping conditions. Interestingly, total magnetic anisotropy energy (C-MAE + D-MAE) at $\Delta n = 1$ is reduced to 0.289 meV/f.u., equivalent to 1.18 Tesla of magnetic field strength. Hence controlling spin alignment and the resulting topological properties of one-electron-doped (per unit cell) ferromagnetic monolayer $CrSiTe_3$ via applying external magnetic field become achievable, which will be discussed further in following section (Sec. 4.3.6).

To investigate more details about suppression of magnetic anisotropy energy under electron doping as depicted in Fig. 4.8(c), we calculate total energy changes induced by varying spin directions as illustrated in Fig. 4.9. Without the change in the electronic structure (*i.e.* when the local spin moment picture is robust), total energy as a function of spin directions should have a form of

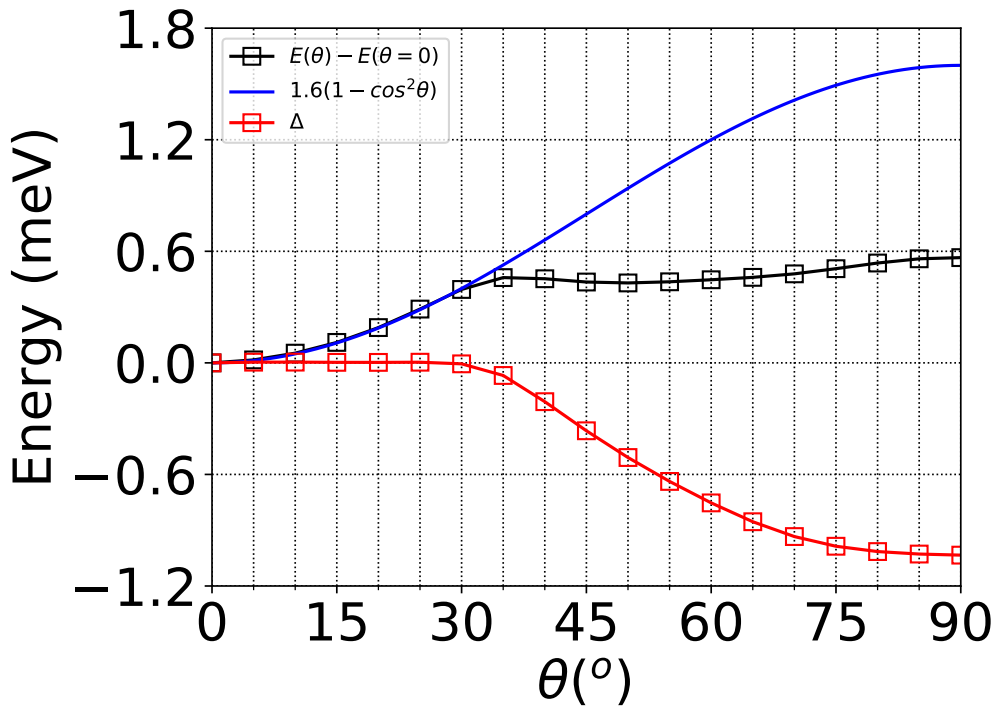

Figure 4.9 (Color online) Total energy as a function of polar angle θ (black line and marker). Zero value is set to be total energy of θ=0. Fitting function of total energy for $0 \leq \theta \leq 30$ (blue line) and difference between total energy and fitting function (red line and marker) are also indicated.

$(\mathbf{M}\cdot\mathbf{z})^2 \sim \cos^2\theta$ (see Fig. 4.10 for the angle and vector definition). Such trend is maintained until θ is increased up to 30°, and beyond that the anisotropy energy starts to deviate from the simple local moment picture. This implies an onset of additional terms that comes into play to favor easy-plane configurations around $\theta = 30°$, which turns out to originates from the evolution of the electronic structure with respect to θ (see below the discussion on Fig. 4.11 for more detailed discussion). As a result, shape of total energy shows local minimum near $\theta \sim 50°$ and magnitude of magnetic anisotropy energy is suppressed about 1 meV at $\theta = 90°$ in fig. 4.9.

# of doping electron (Δn)	magnetic moment (μ_B)	C-MAE (meV/f.u.)	D-MAE (meV/f.u.)
0.0	3.97	1.378	-0.244
0.5	4.10	0.101	-0.260
1.0	4.23	0.566	-0.277
1.5	4.37	-0.665	-0.295
2.0	4.51	0.085	-0.314

Table 4.2 Magnetic moment and anisotropy energies for each number of doping electrons in unit cell. Magnetocrystalline anisotropy energy (C-MAE) is energy difference between easy axis and easy plane spin configuration which was estimated by DFT calculations. Magnetic dipolar anisotropy energy (D-MAE) is magnetic dipole-dipole interaction energy. (+) sign indicate preference of out-of-plane spin directions. All calculation are performed with fixed lattice constant as 7.0 Å.

4.3.6 Switching AHC via External Magnetic Fields

Because magnetic anisotropy energy of Cr e_g bands in the presence of one electron doping conditions is small enough to tune the FM via external fields, we investigate the behavior of AHC as the spin orientation direction is changed

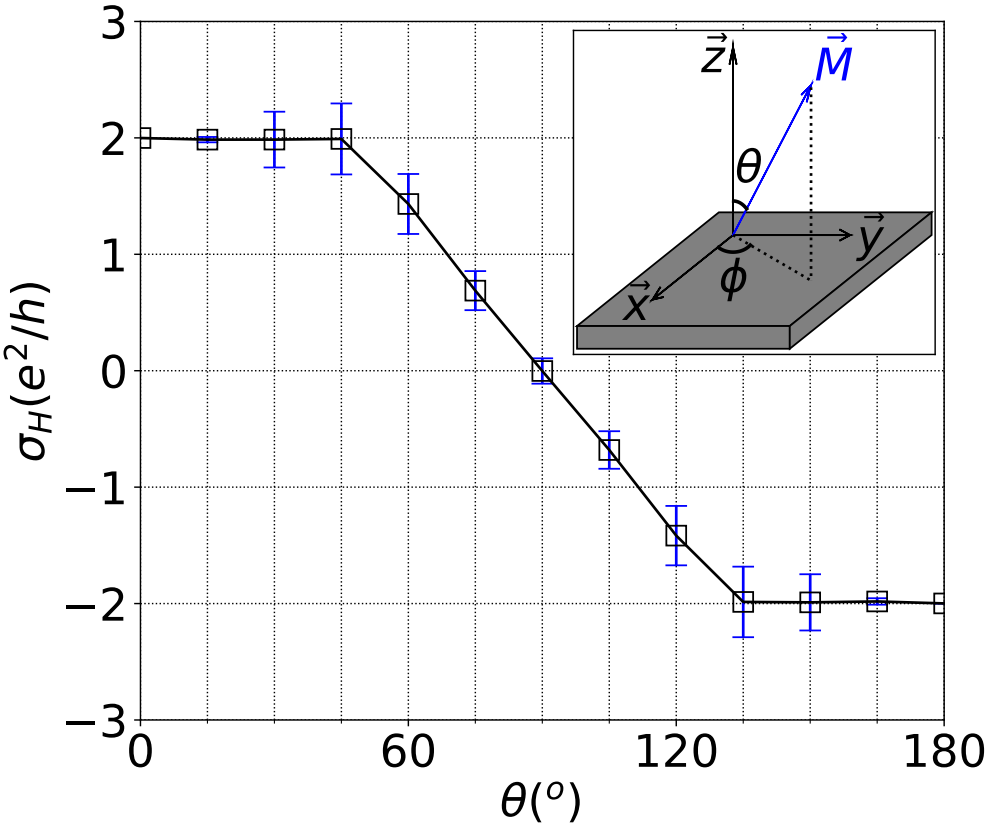

Figure 4.10 (Color online) Azimuthal spin angle (ϕ) averaged AHC for one electron doped $CrSiTe_3$ as a function of polar angle (θ). Mean value (black line with square marker) and standard deviation (blue errorbar) of AHC for each θ are remarked. Upper right panel shows polar angle (θ) and azimuthal spin angle (ϕ) of magnetization vector (blue arrow) and $CrSiTe_3$ monolayer as gray slab.

from out-of-plane to in-plane direction. Fig. 4.10 shows the magnitude of AHC, averaged over the azimuthal angle ϕ of the net magnetization, as a function of polar angle θ of the FM spin orientation with respect to the layer-normal direction. From $\theta = 0^\circ$ to $\theta = 45^\circ$, AHC remains quantized at $2e^2/h$ where there are deviations with respect to azimuthal spin angle ϕ. Surprisingly, as θ is increased further, AHC begins to reduce and goes to almost zero at $\theta = 90^\circ$. We also confirm anti-symmetric behavior of AHC as a function of spin polar angle θ. One can imagine that spin directions for $\theta = 180^\circ$ is opposite to $\theta = 0^\circ$ so that rotation of corresponding chiral edge modes are reversed, i.e. clockwise to counterclockwise. Because the direction of the FM moment can be switched between out-of-plane and in-plane via external magnetic fields at one electron doping per unit cell, the quantum anomalous Hall phase at this doping can also be switched on-off via external magnetic fields of about 1.18 Tesla estimated in previous Sec. 4.3.5.

To show the changes of band features and AHC at one electron doping as the net magnetization is tilted, we plotted Berry curvatures in the BZ and along the e_g band dispersion with tilting the spin orientation direction as summarized in Fig. 4.11. Note that here we set spin azimuthal angle $\phi = 0$ for the plotting of Berry curvatures and band structures. As θ is increased electron and hole pockets start to develop, close to $\theta = 30^\circ$, in the middle of Γ-$M_{1,2,3}$ lines and around $M_{1,3}$ points (see Fig. 4.11(b) and (c)). Especially, the presence of hole pockets and its expansion contribute to the reduction of the AHC as θ is increased beyond 30$\sim$45° (compare with Fig. 4.10), while AHC contributions from electron pockets around $M_{1,3}$ points are almost vanishing.

As θ is further increased beyond 60°, sign of Berry curvature distribution around M_1 and M_3 points are flipped (compare Fig. 4.11(g) with (i) an

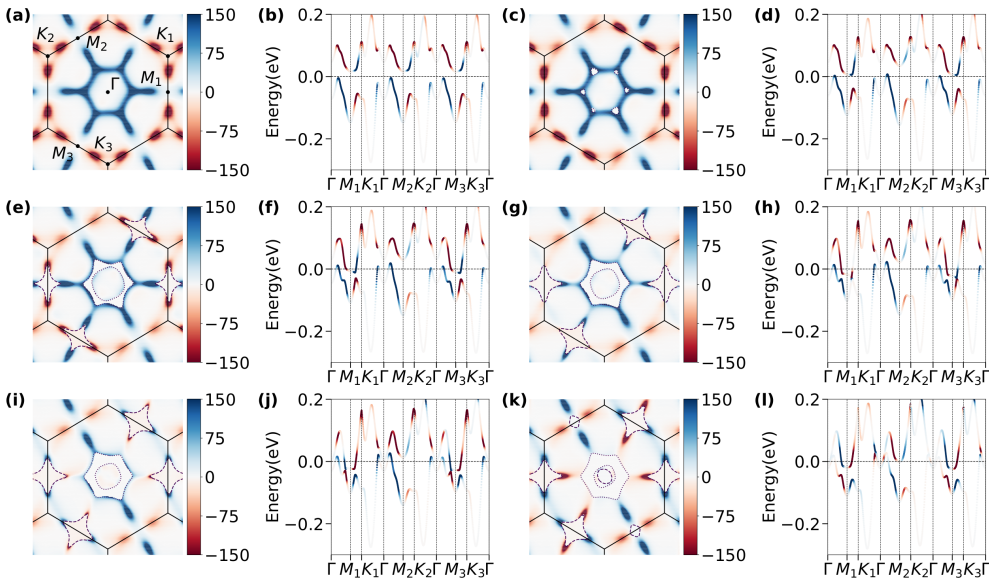

Figure 4.11 (Color online) (a,c,e,g,i,k) Plots of Berry curvature distribution originating from occupied Cr e_g states in the momentum space (unit in $\mathring{A}^2$) and (b,d,f,h,j,l) Berry-curvature-projected band structures of Cr e_g bands along the high symmetry lines with increasing polar angle (θ). In Berry curvature plots (a,c,e,g,i,k) dotted and dashed lines depict Fermi surfaces of lowest and second lowest bands, respectively. High symmetry points are marked in panel (a). Polar angle for each case is (a,b) $\theta = 0°$, (c,d) $\theta = 30°$, (e,f) $\theta = 45°$, (g,h) $\theta = 60°$, (i,j) $\theta = 75°$ and (k,l) $\theta = 90°$. Azimuthal angle of $\phi = 0°$ for the magnetization direction and one electron doping per unit cell are adopted for all cases.

(k)). This is attributed to the band touching below the Fermi level and the resulting sign reversal of Berry curvature of occupied bands. Comparing panel Fig. 4.11(h), (i), and (l), it can be noticed that band crossings occur on Γ-M_1 and Γ-M_3 lines, slightly below the Fermi level, around $\theta = 75°$. The crossings give rise to sign flipping of the Berry curvature of involved bands in the vicinity of the crossing point, which leads to cancellation of net Berry curvature and vanishing AHC at $\theta = 90°$.

In addition, note that the band gap between highest-occupied and lowest-unoccupied bands at Γ is suppressed as θ is increased, so that at $\theta = 90°$ the quadratic band touching is restored. This features are depicted in Fig. 4.12. Schematic band pictures are almost same under the variations of spin angle, whereas the distance of the e_{g} bands manifold become closer to each other. Therefore, it can give rise to band touching in the e_{g} bands manifold which is origin of changing of Chern numbers as described in Fig. 4.11(b-g). At $\theta = 90°$ (Fig. 4.11(g)), tiny band gap energy remains at Γ and K_2 points despite vanishing of SOC effect. This is because out-of-spin components slightly arise from the process of convergence step in DFT calculations. In addition, higher order terms in Hamiltonian also serve to removing degeneracy of e_{g} bands manifold so that Chern numbers can be still defined and computed even under the condition of easy-plane spin configurations. This occurs because *i)* the bands close to the Γ point consist mostly of Te $p_{x,y}$-orbitals, and *ii)* SOC in the presence of FM behaves as an orbital Zeeman fields $\lambda_{\mathrm{SO}}\mathbf{m}\cdot\hat{\mathbf{L}}$ (λ_{SO} and $\mathbf{m}$ being SOC strength and net magnetization, respectively). When $\mathbf{m} = m_z\mathbf{z}$ the $\lambda_{\mathrm{SO}}m_z\hat{L}_z$ splits the $p_{x,y}$ doublet into $\hat{L}_z$ eigenstates ($p_x \pm ip_y$), but when $\mathbf{m}$ is in-plane the splitting cannot occur due to the absence of p_z character. Hence

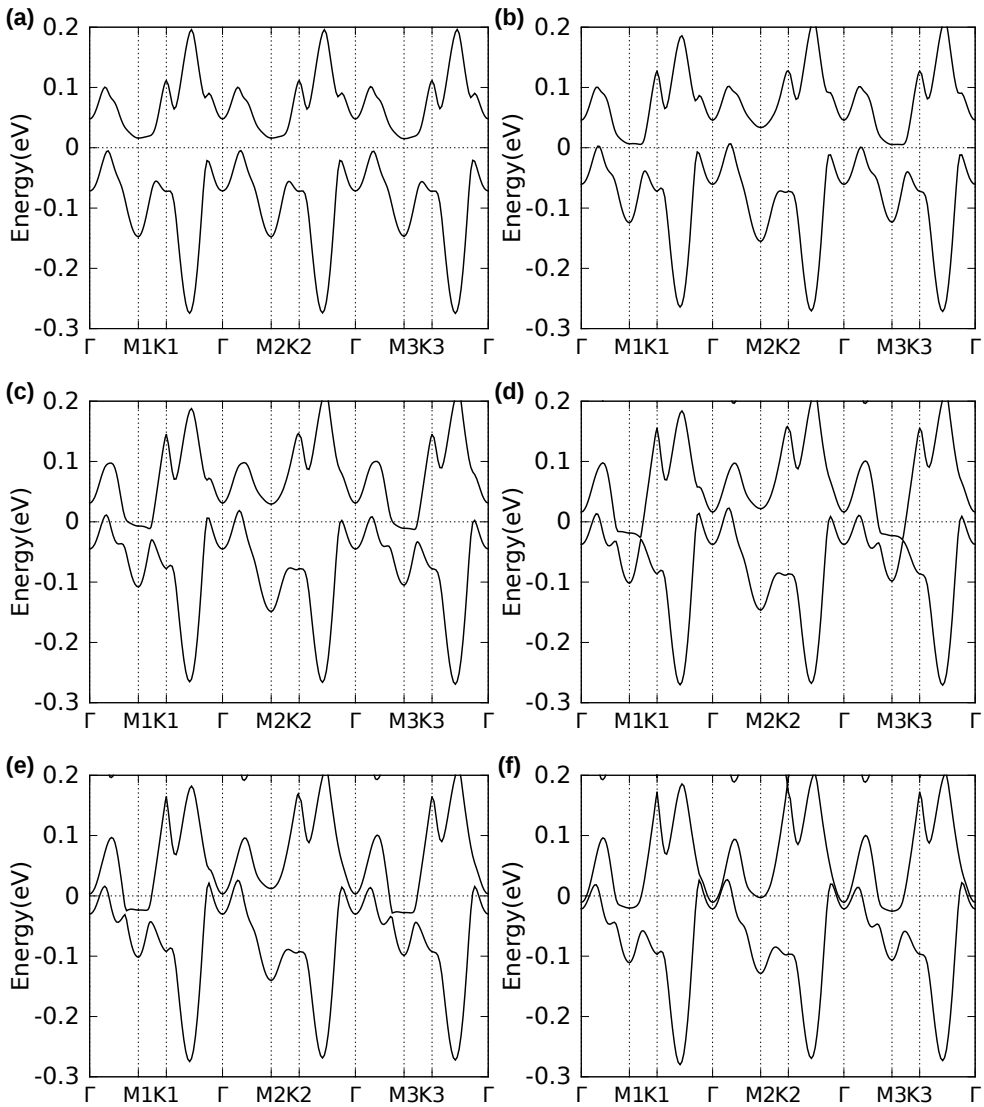

Figure 4.12 Band structure of lowest and second lowest Cr e_g bands under one electron doping in unit cell and considering SOC effect by varying spin angle (θ). (a) $\theta = 0°$, (b) $\theta = 30°$, (c) $\theta = 45°$, (d) $\theta = 60°$, (e) $\theta = 75°$, (f) $\theta = 90°$, respectively.

tilting the spin direction leads to the quenching of SOC in the vicinity of Γ point.

Lastly, we discuss the relation between the change of Fermi surface topology and the magnetic anisotropy. Fig. 4.13 shows the orbital-angular-momentum-projected band structures as θ is increased from 0 to 90°. At each k point of band structures, we calculate $\langle L_z^2 \rangle$ and $\langle L_x^2 \rangle$ for Cr d orbitals and Te p orbitals using following relations. ($\hbar^2$ is omitted)

$$\begin{aligned}
L_z^2|p_z\rangle = 0, L_z^2|p_x\rangle = |p_x\rangle, L_z^2|p_y\rangle = |p_y\rangle \\
L_z^2|d_{z^2}\rangle = 0, L_z^2|d_{x^2-y^2}\rangle = 4|d_{x^2-y^2}\rangle \\
L_z^2|d_{xy}\rangle = 4|d_{xy}\rangle, L_z^2|d_{yz}\rangle = |d_{yz}\rangle, L_z^2|d_{zx}\rangle = |d_{zx}\rangle \\
L_x^2|p_z\rangle = |p_z\rangle, L_x^2|p_x\rangle = 0, L_x^2|p_y\rangle = |p_y\rangle \\
L_x^2|d_{z^2}\rangle = 3|d_{z^2}\rangle + \sqrt{3}|d_{x^2-y^2}\rangle, L_x^2|d_{x^2-y^2}\rangle = \sqrt{3}|d_{z^2}\rangle + 3|d_{x^2-y^2}\rangle \\
L_x^2|d_{xy}\rangle = |d_{xy}\rangle, L_x^2|d_{yz}\rangle = 4|d_{yz}\rangle, L_x^2|d_{zx}\rangle = |d_{zx}\rangle
\end{aligned} \tag{4.9}$$

Definition of basis set d orbitals and Te p orbitals are listed as followed.

$$\begin{aligned}
|d_{z^2}\rangle &= |L=2, L_z=0\rangle \\
|d_{x^2-y^2}\rangle &= \frac{1}{\sqrt{2}}(|L=2, L_z=-2\rangle + |L=2, L_z=2\rangle) \\
|d_{xy}\rangle &= \frac{i}{\sqrt{2}}(|L=2, L_z=-2\rangle - |L=2, L_z=2\rangle) \\
|d_{yz}\rangle &= \frac{i}{\sqrt{2}}(|L=2, L_z=-1\rangle + |L=2, L_z=1\rangle) \\
|d_{zx}\rangle &= \frac{1}{\sqrt{2}}(|L=2, L_z=-1\rangle - |L=2, L_z=1\rangle)
\end{aligned} \tag{4.10}$$

$$\begin{aligned}
|p_z\rangle &= |L=1, L_z=0\rangle \\
|p_x\rangle &= \frac{1}{\sqrt{2}}(|L=1, L_z=1\rangle + |L=1, L_z=-1\rangle) \\
|p_y\rangle &= \frac{i}{\sqrt{2}}(|L=1, L_z=1\rangle - |L=1, L_z=-1\rangle)
\end{aligned} \tag{4.11}$$

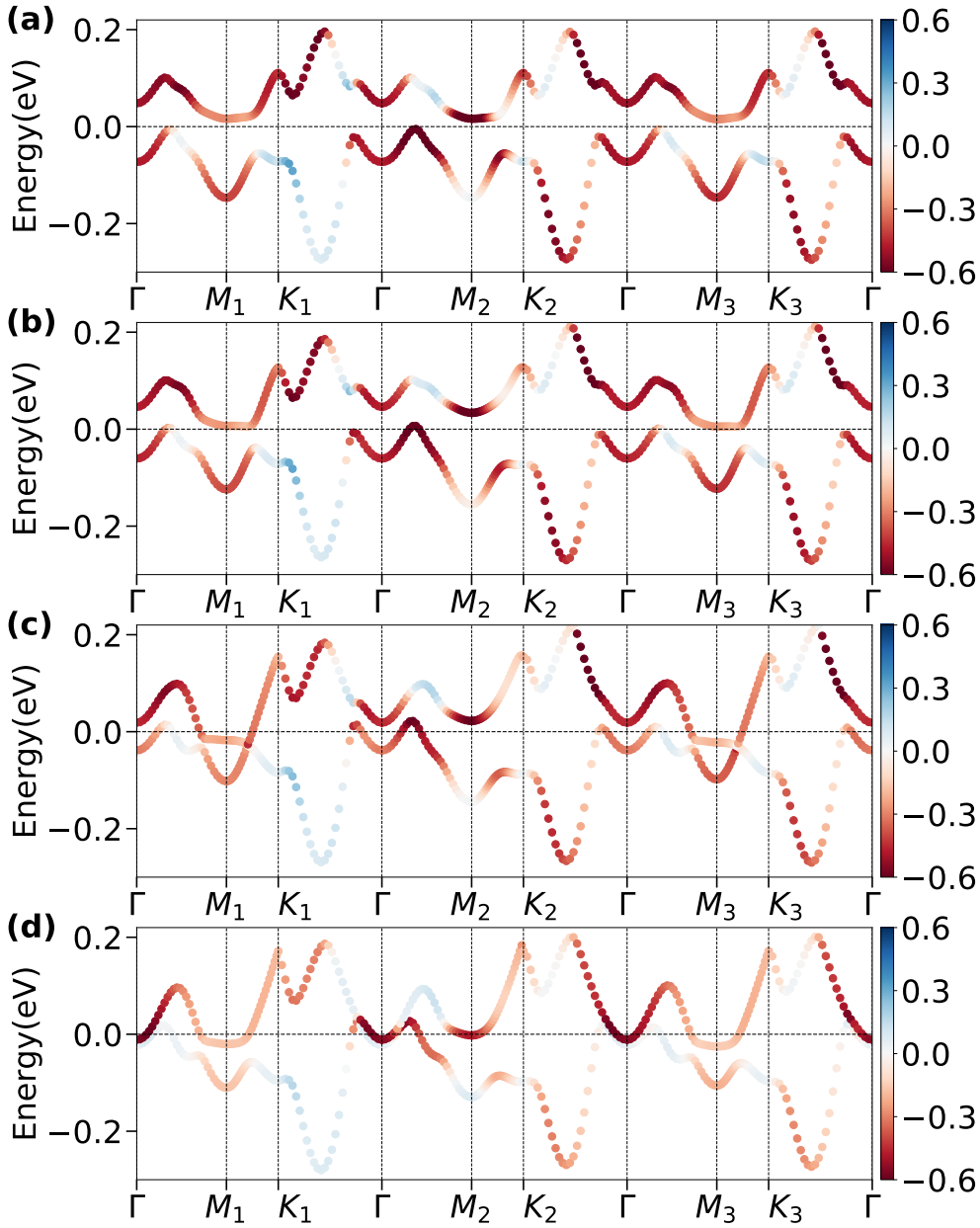

Figure 4.13 (Color online) L^2-projected band structures with (a) $\theta = 0°$, (b) $\theta = 30°$, (c) $\theta = 60°$, and (d) $\theta = 90°$, where intensity and color of dots represent a difference between L_z^2- and L_x^2-character ($\langle L_z^2 \rangle$ - $\langle L_x^2 \rangle$) of each Bloch state (blue and red color indicating preference of out-of-plane and in-plane orbital angular momenta, respectively.)

where atomic p orbitals is represented by combination of spherical harmonics of $L = 1$ and When $\theta > 30°$, electron pockets with dominant in-plane orbital angular momentum (red color in the figures) start to develop near M_1 and M_3 points, while the hole pockets on the Γ-M lines bear weak orbital momentum. Such change of Fermi surface topology and enhanced in-plane orbital momentum character of occupied bands strengthens the in-plane magnetic anisotropy energy ($\propto L_x^2$), leading to deviation from local moment behavior of the energy cost with respect to spin tilting (*i.e.* the $1 - \cos\theta$ dependence of the energy cost in Fig. 4.9) beyond $\theta = 30°$ and preference toward in-plane anisotropy of the system.

In electronic band structure, SOC band gap energy is affected by spin orientation angle shown in Sec. 4.3.6. Size of band gap energy is determined by off diagonal term of Hamiltonian matrix so that SOC band gap energy could be estimated by calculating components of $H_{SO} = \lambda_{SO} L \cdot S$ matrix. SOC Hamiltonian could be represented as matrix form by choosing relevant basis set as atomic p orbitals $|p_{i,\sigma}\rangle$ because dominant SOC effect comes from heavy Te atoms where i is coordinates and σ is spin index, respectively. Components of SOC matrix and basis set can be written as

$$H_{i,j} = \lambda_{SO} \langle p_{i,\sigma} | L_x S_x + L_y S_y + L_z S_z | p_{j,\sigma'} \rangle \tag{4.12}$$

If we choose basis set as $|p_{x,\uparrow}\rangle$, $|p_{y,\uparrow}\rangle$, $|p_{z,\uparrow}\rangle$, $|p_{x,\downarrow}\rangle$, $|p_{y,\downarrow}\rangle$, $|p_{z,\downarrow}\rangle$, $L{\cdot}S$ matrix is equal to Eq. (4.13).

$$L{\cdot}S = \begin{pmatrix} 0 & -i & 0 & 0 & 0 & -1 \\ i & 0 & 0 & 0 & 0 & -i \\ 0 & 0 & 0 & 1 & i & 0 \\ 0 & 0 & 1 & 0 & -i & 0 \\ 0 & 0 & -i & i & 0 & 0 \\ -1 & i & 0 & 0 & 0 & 0 \end{pmatrix} \tag{4.13}$$

However, $L{\cdot}S$ matrix changes to Eq. (4.14) when basis set is $|p_{x,+}\rangle$, $|p_{y,+}\rangle$, $|p_{z,+}\rangle$, $|p_{x,-}\rangle$, $|p_{y,-}\rangle$, $|p_{z,-}\rangle$, where + and - indicate up-spin and down-spin along x axis. Definition of p orbitals are listed in Eq. (4.11). ($\hbar$ is omitted)

$$L{\cdot}S = \begin{pmatrix} 0 & 0 & 0 & 0 & -i & 1 \\ 0 & 0 & -i & i & 0 & 0 \\ 0 & i & 0 & -1 & 0 & 0 \\ 0 & -i & -1 & 0 & 0 & 0 \\ i & 0 & 0 & 0 & 0 & -i \\ 1 & 0 & 0 & 0 & i & 0 \end{pmatrix} \tag{4.14}$$

Above matrices are calculated by using followed relations of angular momentum and spin operators.

$$L_z|p_x\rangle = i|p_y\rangle, L_z|p_y\rangle = -i|p_x\rangle, L_z|p_z\rangle = 0 \tag{4.15}$$

$$L_x|p_x\rangle = 0, L_x|p_y\rangle = i|p_z\rangle, L_x|p_z\rangle = -i|p_y\rangle \tag{4.16}$$

$$L_y|p_x\rangle = i|p_z\rangle, L_y|p_y\rangle = 0, L_y|p_z\rangle = -i|p_x\rangle \tag{4.17}$$

$$S_z|\uparrow\rangle = |\uparrow\rangle, S_z|\downarrow\rangle = |\downarrow\rangle \tag{4.18}$$

$$S_x|\uparrow\rangle = |\downarrow\rangle, S_x|\downarrow\rangle = |\uparrow\rangle \tag{4.19}$$

$$S_y|\uparrow\rangle = i|\downarrow\rangle, S_y|\downarrow\rangle = -i|\uparrow\rangle \tag{4.20}$$

$$S_z|+\rangle = |-\rangle, S_z|-\rangle = |+\rangle \tag{4.21}$$

$$S_x|+\rangle = |+\rangle, S_x|-\rangle = |-\rangle \tag{4.22}$$

$$S_y|+\rangle = -i|-\rangle, S_y|-\rangle = i|+\rangle \tag{4.23}$$

At Γ point, p_x and p_y orbitals are hybridized with e_g band manifolds, off diagonal term of SOC Hamiltonian matrix $\langle p_x|L{\cdot}S|p_y\rangle$ determine bandgap energy. Therefore, bands split due to SOC effect for basis with out-of-plane spin direction ($\langle p_{x,\uparrow}|L{\cdot}S|p_{y,\uparrow}\rangle \neq 0$. However, band gap is closing for basis with in-plane spin direction ($\langle p_{x,+}|L{\cdot}S|p_{y,+}\rangle = 0$ indicating SOC effect disappear.

4.3.7 Effect of Electron Doping to Exchange Interaction

In this section, we discuss magnetic exchange interaction of $CrSiTe_3$ monolayer in the presence of electron doping. In Fig. 3.6 and Fig. 4.2, total energy difference among various magnetic configuration changes as a function of electron doping in unit cell. This total energy difference between FM and AFM states is related to exchange parameters which determine Curie temperature. To analyze the exchange interaction of $CrSiTe_3$ monolayer, we construct magnetic Hamiltonian using Heisenberg model up to third nearest neighbor(NN) written by[6]

$$H = \sum_{NN} J_1 S^2 + \sum_{2_{nd}NN} J_2 S^2 + \sum_{3_{rd}NN} J_3 S^2, \tag{4.24}$$

where J_i is i_{th} NN exchange parameters and S is magnitude of magnetic moment, respectively. Using Eq. 4.24, total energies of FM and various AFM

states with zigzag, Neel, stripy type are represented by following expressions,

$$\begin{aligned} E(FM) &= E^{(0)} + 3J_1S^2 + 6J_2S^2 + 3J_3S^2 \\ E(AF_{zigzag}) &= E^{(0)} + J_1S^2 - 2J_2S^2 - 3J_3S^2 \\ E(AF_{Neel}) &= E^{(0)} - 3J_1S^2 + 6J_2S^2 - 3J_3S^2 \\ E(AF_{stripy}) &= E^{(0)} - J_1S^2 - 2J_2S^2 + 3J_3S^2 \end{aligned} \tag{4.25}$$

where $E^{(0)}$ is spin-independent energy term. Using Eq. (4.25) and our total energy calculation results, we estimate exchange parameters as a function of electron doping listed in table 4.3.

# of doping electron (Δn)	J_1	J_2	J_3
0.0	-14.735	0.199	1.568
1.0	-4.807	-1.035	-12.961
2.0	-0.123	-0.692	-0.729

Table 4.3 Exchange parameters of NN, second NN and third NN hoping for various doping electrons in unit cell. Unit of exchange parameters is meV.

At one electron doping in unit cell, all three exchange parameters favor ferromagnetism where there is only NN ferromagnetic exchange in pristine case. Therefore, the ferromagnetism is much more stabilized under one electron doping and this enhanced ferromagnetic exchange interaction will increases Curie temperature of $CrSiTe_3$ monolayer. When electron doping further increases to two electron in unit cell, ferromagnetic exchange is still favored where the magnitudes of all three exchange parameters are decreased to order of 0.1 meV. As a result, the magnetic state will be close to Heisenberg type with weak ferromagnetism near two electron doping in unit cell.

4.4 Conclusion

We study electronic and topological properties of electron doped single layer structure of $CrSiTe_3$ by performing first principle calculation based on density functional theory (DFT). Lattice constant and Hubbard U parameters are fixed by confirming FM ground state and topological characters are invariant under certain conditions. We construct MLWF which is Fourier transform of Kohn-Sham wavefunctions of each bands and calculate Berry curvatures for analysis of topological characters using converged MLWF. Nontrivial topology appear within Cr e_g bands manifold which can leads to Chern insulating phases in $CrSiTe_3$. Chiral edge modes are also calculated which is consistent with total Chern number calculations. Moreover, we find spin angle dependent AHC under one electron doping in unit cell, together with suppression of magnetic anisotropy. Additional electrons may enhance Curie temperature of ferromagnetic ordering. Curie temperature is proportional to magnitude of exchange parameters which is determined by energy difference between FM and AFM states. We find that the energy difference between FM and AFM with zigzag configuration increases as electron doping increases by comparing energy diagram described in Fig. 3.6 and Fig. 4.2. One contribution is additional energy gain of Hund coupling in FM states due to extra magnetic moment in e_g orbitals discussed in section 3.3.1. Another contribution is double exchange interactions between partially filled Cr e_g band. As a result, FM state become more stablized under electron doping which increases Curie temperature more beneficial for observing ferromagnetism in $CrSiTe_3$. In order to observe spin angle dependent AHC in experiment, electron doping in unit cell and applying external magnetic field is essential. At one electron doping, total magnetic

anisotropy energy is calculated as 0.289 meV/f.u. which is converted to 1.18 Tesla of magnetic field. For our calculation, one electron doping in unit cell with 7.0Å lattice constant corresponds to carrier density as 2.36×10^{14} cm^{-2}. Ionic liquid gating is representative method of charge doping where order of doping concentration is known as 10^{14} cm^{-2} in 2d systems [84–86]. In recent study, about 2×10^{14} cm^{-2} of average electron doping per one layer is accomplished in $CrGeTe_3$[73], where most of doping electrons are distributed to topmost two layers. In addition, more electrons are confined in topmost layer, which imply the doping concentrations are almost adjacent to our theoretical goal. Because $CrGeTe_3$ has same crystal structure and similar lattice constant with $CrSiTe_3$, we expect our theoretical suggestion of Chern insulating phases and magnetic field dependent QAHE can be realized. Therefore, we expect $CrSiTe_3$ can be a Chern insulator with high Chern numbers controlled by external magnetic field by applying external magnetic field and ionic liquid gating. Furthermore, the overall band character and crossing points of Cr e_g bands manifold in $CrGeTe_3$ is almost same with $CrSiTe_3$ as shown in Fig. 3.7. The only difference is that the band overlap of Cr e_g bands is more complicated in $CrGeTe_3$ case. This makes more difficult to calculate Berry curvature and analyze toplogical properties. However, the lowest band of Cr e_g bands does not touch with other bands so that topological characters may remain. Therefore, we expect that Chern insulating phases discussed previous section also emerge in $CrGeTe_3$ monolayer under one electron doping in unit cell.

Chapter 5

Summary and Perspective

By using openMX code based on DFT calculations within the GGA+U method, we investigate electronic, magnetic and topological properties of $CrSiTe_3$ compounds. We compare total energy for various magnetic configurations of $CrSiTe_3$ and $CrGeTe_3$ compounds. We find that the magnetic ground state depends on the choice of Hubbard U parameters in $CrSiTe_3$ monolayer. In addition, band gap energy and interlayer magnetic interaction energy also depends on the U value, which indicates on-site Coulomb interaction play a crucial role in $CrSiTe_3$ and $CrGeTe_3$ compounds. The interlayer magnetic interaction energy shrinks for near $U = 1.0$ eV, which is relevant to properties of layered materials with interlayer van der Waals bonding. Furthermore, selection of U near 1.0 eV makes good agreement with photoemission spectrum experiment result of $CrGeTe_3$[70]. Under $U = 1.5$ eV, $CrSiTe_3$ and $CrGeTe_3$ have ferromagnetic ground state, where the strong $dp\sigma$-hybridization between Cr e_g - Te p orbitals is crucial for the stabilization of ferromagnetic ordering of Cr ions. Meanwhile, we find crossing points including multiple Dirac cones and quadratic dispersion within Cr e_g conduction manifolds. By considering SOC effect, the crossings are lifted which leads to nontrivial topology bands with high Chern numbers.

Chiral edge modes are also calculated which is consistent with our Chern number and Berry curvature calculation results. We calculate the AHC as a function of electron doping, where it is quantized at integer electron doping in unit cell. We focus on the one electron doping concentration in unit cell and find spin angle dependent AHC together with suppression of magnetic anisotropy. For our calculation, one-electron doping in the formula unit cell with 7.0Å lattice constant corresponds to carrier density as 2.36×10^{14} cm^{-2}. Ionic liquid gating is representative method of charge doping where order of doping concentration is known as 10^{14} cm^{-2} in 2D systems [84–86]. In recent study, about 4×10^{14} cm^{-2} of electron doping concentration is accomplished in $CrGeTe_3$[73] where most doping electrons are confined at topmost layer. This is almost adjacent to our theoretical goal. Because $CrGeTe_3$ has the same crystal structure and similar lattice constant as $CrSiTe_3$, we expect our theoretical suggestion of Chern insulating phases and magnetic field dependent QAHE can be realized as discussed throughout previous section. We hope that our theoretical findings serve for attracting people's interest of $CrSiTe_3$, which activate the experimental research of exfoliating the $CrSiTe_3$ down to atomically thin film together with observing magnetism and also anomalous Hall conductivity.

Bibliography

[1] Geim, A. K.; Novoselov, K. S. *Nat. Mater.* **2007**, *6*, 183–191.

[2] Giovannetti, G.; Khomyakov, P. A.; Brocks, G.; Kelly, P. J.; van den Brink, J. *Phys. Rev. B* **2007**, *76*, 073103.

[3] Dean, C. R.; Young, A. F.; Meric, I.; Lee, C.; Wang, L.; Sorgenfrei, S.; Watanabe, K.; Taniguchi, T.; Kim, P.; Shepard, K. L.; Hone, J. *Nat. Nanotechnol.* **2010**, *5*, 722–726.

[4] Wang, Q.; Kalantar-Zadeh, K.; Kis, A.; Coleman, J.; Strano, M. *Nat. Nanotechnol.* **2012**, *7*, 699–712.

[5] Mak, K.; He, K.; Shan, J. *Nat. Nanotechnol.* **2012**, *7*, 494–498.

[6] Sivadas, N.; Daniels, M. W.; Swendsen, R. H.; Okamoto, S.; Xiao, D. *Phys. Rev. B* **2015**, *91*, 235425.

[7] Lee, J.-U.; Lee, S.; Ryoo, J. H.; Kang, S.; Kim, T. Y.; Kim, P.; Park, C.-H.; Park, J.-G.; Cheong, H. *Nano Lett.* **2016**, *16*, 7433–7438.

[8] Li, X.; Yang, J. *J. Mater. Chem. C* **2014**, *2*, 7071–7076.

[9] Wildes, A. R.; Simonet, V.; Ressouche, E.; McIntyre, G. J.; Avdeev, M.; Suard, E.; Kimber, S. A. J.; Lan çon, D.; Pepe, G.; Moubaraki, B.; Hicks, T. J. *Phys. Rev. B* **2015**, *92*, 224408.

[10] Long, G.; Henck, H.; Gibertini, M.; Dumcenco, D.; Wang, Z.; Taniguchi, T.; Watanabe, K.; Giannini, E.; Morpurgo, A. F. *Nano Lett.* **2020**, *20*, 2452–2459.

[11] Gong, C.; Li, L.; Li, Z.; Ji, H.; Stern, A.; Xia, Y.; Cao, T.; Bao, W.; Wang, C.; Wang, Y.; Qiu, Z.; Cava, R.; Louie, S.; Xia, J.; Zhang, X. *Nature* **2017**, *546*, 265–269.

[12] Huang, B.; Clark, G.; Navarro-Moratalla, E.; Klein, D. R.; Cheng, R.; Seyler Kyle, L.; Zhong, D.; Schmidgall, E.; McGuire, M. A.; Cobden, D. H.; Yao, W.; Xiao, D.; Jarillo-Herrero, P.; Xu, X. *Nature* **2017**, *546*, 270–273.

[13] Mermin, N. D.; Wagner, H. *Phys. Rev. Lett.* **1966**, *17*, 1133–1136.

[14] Haldane, F. D. M. *Phys. Rev. Lett.* **1988**, *61*, 2015–2018.

[15] Garrity, K. F.; Vanderbilt, D. *Phys. Rev. B* **2014**, *90*, 121103.

[16] Chen, P.; Zou, J.-Y.; Liu, B.-G. *Phys. Chem. Chem. Phys.* **2017**, *19*, 13432–13437.

[17] Niu, C.; Hanke, J.-P.; Buhl, P.; Bihlmayer, G.; Wortmann, D.; Blugel, S.; Mokrousov, Y. *arXiv* **2017**.

[18] Kalesaki, E.; Delerue, C.; Morais Smith, C.; Beugeling, W.; Allan, G.; Vanmaekelbergh, D. *Phys. Rev. X* **2014**, *4*, 011010.

[19] Jiang, H.; Qiao, Z.; Liu, H.; Niu, Q. *Phys. Rev. B* **2012**, *85*, 045445.

[20] Song, Y.-J.; Ahn, K.-H.; Pickett, W. E.; Lee, K.-W. *Phys. Rev. B* **2016**, *94*, 125134.

[21] Xiong, T.-S.; Gong, J.; An, J.-H. *Phys. Rev. B* **2016**, *93*, 184306.

[22] Baidya, S.; Yu, J.; Kim, C. H. *Phys. Rev. B* **2018**, *98*, 155148.

[23] Baidya, S.; Kang, S.; Kim, C. H.; Yu, j. *Sci. Rep.* **2019**, *9*, 13807.

[24] Sugita, Y.; Miyake, T.; Motome, Y. *Phys. Rev. B* **2018**, *97*, 035125.

[25] Liu, J.; Park, S. Y.; Garrity, K. F.; Vanderbilt, D. *Phys. Rev. Lett.* **2016**, *117*, 257201.

[26] Mao, N.; Hu, X.; Wang, H.; Dai, Y.; Huang, B.; Mokrousov, Y.; Niu, C. *Phys. Rev. B* **2021**, *103*, 195152.

[27] Hu, C.; Lien, S.-W.; Feng, E.; Mackey, S.; Tien, H.-J.; Mazin, I. I.; Cao, H.; Chang, T.-R.; Ni, N. *Phys. Rev. B* **2021**, *104*, 054422.

[28] Jin, Y.; Zeng, X.-T.; Feng, X.; Du, X.; Wu, W.; Sheng, X.-L.; Yu, Z.-M.; Zhu, Z.; Yang, S. A. *Phys. Rev. B* **2021**, *104*, 165424.

[29] Zhang, H.; Liu, C.-X.; Qi, X.-L.; Dai, X.; Fang, Z.; Zhang, S.-C. *Nat. Phys.* **2009**, *5*, 438–442.

[30] Kyriienko, O.; Kibis, O. V.; Shelykh, I. A. *Phys. Rev. B* **2019**, *99*, 115411.

[31] Chen, X.; Qi, J.; Shi, D. *Phys. Lett. A* **2015**, *379*, 60–63.

[32] Lin, M.-W.; Zhuang, H. L.; Yan, J.; Ward, T. Z.; Puretzky, A. A.; Rouleau, C. M.; Gai, Z.; Liang, L.; Meunier, V.; Sumpter, B. G.; Ganesh, P.; Kent, P. R. C.; Geohegan, D. B.; Mandrus, D.; Xiao, K. *J. Mater. Chem. C* **2016**, *4*, 315–322.

[33] Williams, T. J.; Aczel, A. A.; Lumsden, M. D.; Nagler, S. E.; Stone, M. B.; Yan, J.-Q.; Mandrus, D. *Phys. Rev. B* **2015**, *92*, 144404.

[34] Hohenberg, P.; Kohn, W. *Phys. Rev.* **1964**, *136*, B864–B871.

[35] Kohn, W.; Sham, L. J. *Phys. Rev.* **1965**, *140*, A1133–A1138.

[36] Perdew, J. P.; Zunger, A. *Phys. Rev. B* **1981**, *23*, 5048–5079.

[37] Ceperley, D. M.; Alder, B. J. *Phys. Rev. Lett.* **1980**, *45*, 566–569.

[38] Perdew, J. P.; Burke, K.; Ernzerhof, M. *Phys. Rev. Lett.* **1996**, *77*, 3865–3868.

[39] Anisimov, V. I.; Zaanen, J.; Andersen, O. K. *Phys. Rev. B* **1991**, *44*, 943–954.

[40] Hubbard, J. *Proc. R. Soc. Lond.* **1963**, *276*, 238–257.

[41] Fradkin, E. *Field theories of condensed matter physics* **Westview, 1998**.

[42] Elenewski, J. E.; Hackett, J. C. *J. Chem. Phys.* **2012**, *137*, 124311–124311.

[43] Anisimov, V. I.; Solovyev, I. V.; Korotin, M. A.; Czy żyk, M. T.; Sawatzky, G. A. *Phys. Rev. B* **1993**, *48*, 16929–16934.

[44] Solovyev, I. V.; Dederichs, P. H.; Anisimov, V. I. *Phys. Rev. B* **1994**, *50*, 16861–16871.

[45] Dudarev, S. L.; Botton, G. A.; Savrasov, S. Y.; Humphreys, C. J.; Sutton, A. P. *Phys. Rev. B* **1998**, *57*, 1505–1509.

[46] Barth, U. v.; Hedin, L. *J. Phys. C:Solid State Phys.* **1972**, *5*, 1629–1642.

[47] Kubler, J.; Hock, K.-H.; Sticht, J.; Williams, A. R. *J. Phys. F: Met. Phys.* **1988**, *18*, 469–483.

[48] Wannier, G. H. *Phys. Rev.* **1937**, *52*, 191–197.

[49] Marzari, N.; Vanderbilt, D. *Phys. Rev. B* **1997**, *56*, 12847–12865.

[50] Kang, S.; Kang, S.; Yu, J. *J. Electron. Mater.* **2019**, *48*, 1441–1445.

[51] McGuire, M. A.; Dixit, H.; Cooper, V. R.; Sales, B. C. *Chem. Mater.* **2015**, *27*, 612–620.

[52] Wiedenmann, A.; Rossat-Mignod, J.; Louisy, A.; Brec, R.; Rouxel, J. *Solid State Commun.* **1981**, *40*, 1067–1072.

[53] Brec, R. *Solid State Ion.* **1986**, *22*, 3–30.

[54] Siberchicot, B.; Jobic, S.; Carteaux, V.; Gressier, P.; Ouvrard, G. *J. Phys. Chem.* **1996**, *100*, 5863–5867.

[55] Wildes, A. R.; Roessli, B.; Lebech, B.; Godfrey, K. W. *J. Phys.: Condens. Matter* **1998**, *10*, 6417.

[56] Joy, P. A.; Vasudevan, S. *Phys. Rev. B* **1992**, *46*, 5425–5433.

[57] Takano, Y.; Arai, N.; Arai, A.; Takahashi, Y.; Takase, K.; Sekizawa, K. *J. Magn. Magn. Mater.* **2004**, *272-276*, E593–E595.

[58] Casto, L. D.; Clune, A. J.; Yokosuk, M. O.; Musfeldt, J. L.; Williams, T. J.; Zhuang, H. L.; Lin, M. .-W.; Xiao, K.; Hennig, R. G.; Sales, B. C.; Yan, J. .-Q.; Mandrus, D. *APL Mater.* **2015**, *3*, 041515.

[59] `http://www.openmx-square.org/`.

[60] Ozaki, T.; Kino, H. *Phys. Rev. B* **2005**, *72*, 045121.

[61] Han, M. J.; Ozaki, T.; Yu, J. *Phys. Rev. B* **2006**, *73*, 045110.

[62] Zhuang, H. L.; Xie, Y.; Kent, P. R. C.; Ganesh, P. *Phys. Rev. B* **2015**, *92*, 035407.

[63] Goodenough, J. B. *Phys. Rev.* **1955**, *100*, 564–573.

[64] Goodenough, J. B. *J. Phys. Chem. Solids* **1958**, *6*, 287–297.

[65] Zener, C. *Phys. Rev.* **1951**, *82*, 403–405.

[66] Wang, L.; Maxisch, T.; Ceder, G. *Phys. Rev. B* **2006**, *73*, 195107.

[67] Lin, G. T.; Zhuang, H. L.; Luo, X.; Liu, B. J.; Chen, F. C.; Yan, J.; Sun, Y.; Zhou, J.; Lu, W. J.; Tong, P.; Sheng, Z. G.; Qu, Z.; Song, W. H.; Zhu, X. B.; Sun, Y. P. *Phys. Rev. B* **2017**, *95*, 245212.

[68] Carteaux, V.; Brunet, D.; Ouvrard, G.; Andre, G. *Journal of Physics: Condensed Matter* **1995**, *7*, 69.

[69] Ji, H.; Stokes, R. A.; Alegria, L. D.; Blomberg, E. C.; Tanatar, M. A.; Reijnders, A.; Schoop, L. M.; Liang, T.; Prozorov, R.; Burch, K. S.; Ong, N. P.; Petta, J. R.; Cava, R. J. *J. Appl. Phys.* **2013**, *114*, 114907.

[70] Suzuki, M.; Gao, B.; Koshiishi, K.; Nakata, S.; Hagiwara, K.; Lin, C.; Wan, Y. X.; Kumigashira, H.; Ono, K.; Kang, S.; Kang, S.; Yu, J.; Kobayashi, M.; Cheong, S.-W.; Fujimori, A. *Phys. Rev. B* **2019**, *99*, 161401.

[71] Marsman, M.; Paier, J.; Stroppa, A.; Kresse, G. *J. Phys. Condens. Matter* **2008**, *20*, 064201.

[72] Li, W.; Walther, C. F. J.; Kuc, A.; Heine, T. *J. Chem. Theory Comput.* **2013**, *9*, 2950–2958.

[73] Verzhbitskiy, I. A.; Kurebayashi, H.; Cheng, H.; Zhou, J.; Khan, S.; Feng, Y. P.; Eda, G. *Nat. Electron.* **2020**, *3*, 460–465.

[74] Kim, J.; Kim, K.-W.; Kim, B.; Kang, C.-J.; Shin, D.; Lee, S.-H.; Min, B.-C.; Park, N. *Nano Lett.* **2020**, *20*, 929–935.

[75] Marzari, N.; Mostofi, A. A.; Yates, J. R.; Souza, I.; Vanderbilt, D. *Rev. Mod. Phys.* **2012**, *84*, 1419–1475.

[76] Weng, H.; Ozaki, T.; Terakura, K. *Phys. Rev. B* **2009**, *79*, 235118.

[77] Wu, Q.; Zhang, S.; Song, H.-F.; Troyer, M.; Soluyanov, A. A. *Comput. Phys. Commun.* **2018**, *224*, 405–416.

[78] Fukui, T.; Hatsugai, Y.; Suzuki, H. *J. Phys. Soc. Japan* **2005**, *74*, 1674–1677.

[79] Fang, C.; Gilbert, M. J.; Dai, X.; Bernevig, B. A. *Phys. Rev. Lett.* **2012**, *108*, 266802.

[80] Ewald, P. *Ann. Phys.* **1921**, *64*, 253–287.

[81] Guo, G. Y.; Temmerman, W.; Ebert, H. *J. Phys. Condens. Matter* **1991**, *3*, 8205–8212.

[82] Tung, J. C.; Guo, G. Y. *Phys. Rev. B* **2007**, *76*, 094413.

[83] Fang, Y.; Wu, S.; Zhu, Z.-Z.; Guo, G.-Y. *Phys. Rev. B* **2018**, *98*, 125416.

[84] Bisri, S. Z.; Shimizu, S.; Nakano, M.; Iwasa, Y. *Adv. Mater.* **2017**, *29*, 1607054.

[85] Vaquero, D.; Clerico, V.; Salvador-Sanchez, J.; Quereda, J.; Diez, E.; Perez-Munoz, A. M. *Micromachines* **2021**, *12*.

[86] Perera, M. M.; Lin, M.-W.; Chuang, H.-J.; Chamlagain, B. P.; Wang, C.; Tan, X.; Cheng, M. M.-C.; Tománek, D.; Zhou, Z. *ACS Nano* **2013**, *7*, 4449–4458.

국 문 초 록

2차원 물질에 대한 연구는 응집물리 분야에서 가장 흥미로운 주제 가운데 하나이다. 최근에는 많은 사람들이 이러한 2차원 물질에서 나타나는 자성을 관측하는 것에 관심을 집중하고 있는데, 그 가운데 전이금속 칼코겐 화합물 혹은 할로겐 화합물은 자성을 갖는 층상구조 물질의 후보군으로 여겨지고 있다. $CrSiTe_3$ 화합물은 전이금속 삼칼코겐 화합물 가운데 하나로서, 벌크 구조가 강자성 및 절연체로서의 성질을 가지고 있음이 보고된 바 있다. 하지만 원자단위의 얇은 두께를 갖는 구조는 아직 실험적으로 보고되지 않았는데, 몇몇 이론 연구들 가운데 자성 바닥 상태를 예측함에 있어서 논쟁이 존재하고 있다. 따라서, 우리는 먼저 제일원리 연구를 통해 $CrSiTe_3$ 화합물의 전자적, 자기적 성질에 대한 이해를 바탕으로 자성 바닥 상태에 대해 밝히려 한다.

논문의 첫번째 장에서는 제일 원리 계산을 통해 2차원 전이금속 삼칼코겐 화합물 $CrSiTe_3$ 및 $CrGeTe_3$의 전자적, 자기적 성질에 대해 규명하였다. 단층 구조의 $CrSiTe_3$ 및 $CrGeTe_3$는 강자성 절연체로서의 성질을 갖는데, Cr e_g 오비탈과 Te p 오비탈 사이의 강한 $dp\sigma$ 혼성결합이 Cr 원자간의 강한 강자성에 중요한 역할을 한다. 우리는 밴드갭과 층간 자성 정렬이 Cr d 오비탈의 쿨롱 상호작용 U에 현저히 의존하는 것을 발견했다. 또한, $CrSiTe_3$ 단층에서 층내의 자성 정렬도 U의 선택에 의존함을 발견했는데, $U = 1.5$ eV 조건에서 강자성을 보였다. $CrSiTe_3$ 및 $CrGeTe_3$ 화합물의 밴드갭은 주요 스핀 성분의 Cr e_g 전도밴드와 Te p 원자가밴드 사이에 형성된다. 페르미 레벨 바로 아래의 주요한 Te p 반결합

특성은 U가 증가함에 따라 밴드갭이 감소하는 특성과 밀접한 관련이 있다. 우리는 에너지-밴드 도표를 통해 ABX_3 형태를 갖는 전이금속 삼칼코겐 화합물의 전자적, 자기적 성질을 설명했다.

논문의 나머지 장에서는 층상 구조 및 강자성을 갖는 전이금속 칼코겐 화합물 $CrSiTe_3$이 단층 구조에서 전자 도핑을 통해 천 부도체 상을 나타냄을 보고하였다. Te p 오비탈과의 강한 혼성 결합으로 인해 스핀 궤도 효과가 일정한 밴드갭을 형성하게 되고, 이는 Cr e_g 전도 밴드에서 높은 천 숫자를 갖는 비자명 위상구조를 발생 시킨다. 우리의 계산은 단위 셀 안에 전자 한개를 추가했을때 (약 2.36×10^{14} cm^{-2} 전자 농도에 해당) 양자 비정상 홀 효과가 나타날수 있음을 보였다. 또한, 전자도핑으로 유도되는 비정상 홀 전도도가 스핀의 방향에 의존하며 이때 자기 이방성 에너지가 줄어드는 현상을 발견했다. 이 결과는 외부 자기장을 인가함으로써 비정상 홀 전도도를 조절할수 있음을 의미하며 이는 스핀궤도 효과의 스핀 방향 의존성과 관련이 있다. 우리는 $CrSiTe_3$을 높은 천 수를 갖는 천 부도체와 외부 자기장에 의해 조절되는 양자 비정상 홀 효과를 실현할 수 있는 흥미로운 물질로써 제안하였다.

주요어: 밀도범함수 이론, 2차원 물질, 전이금속 칼코겐 화합물, 강자성, 베리 곡률, 천 부도체, 양자 비정상 홀 효과

학 번: 2015-20316